# Vortex dynamics and scalar transport in the wake of a flat-plate controlled by a vibrating trailing-edge flap

R.H. Hernández[*], L. Tapia

*LEAF-NL, Departamento de Ingeniería Mecánica, Universidad de Chile, Casilla 2777, Santiago, Chile*

ABSTRACT

We investigate the onset and development of vortical flow disturbances introduced into the wake of a horizontally fixed flat-plate by means of the controlled motion of a trailing edge flap. The vibrating mechanics of the flap allows for the introduction of both impulsive and harmonic weak amplitude velocity disturbances which are propagated downstream into the wake flow of the flat-plate. Quantitative experimental and numerical predictions of both steady and unsteady wake flow velocity resulting from different flapping frequencies are made at low Reynolds numbers ($Re < 10^4$). Frequency response tests of the wake confirmed the existence of two dominant frequencies where the wake flow organises with a particular arrangement of downstream moving vortex structures. Numerical predictions of steady (unforced) and forced wake velocity profiles and kinetic energy profiles are in good agreement with the experimental results. In order to understand practical implications of the dominant vortex structures in scalar transport, we have extended the numerical part of the study solving for the concentration equation of a passive scalar being injected in particular regions of the physical domain. A spatial correlation between the trajectory of vortex structures and the scalar concentration downstream the wake is observed. Moreover, the onset of tip vortex structures produced during the forcing cycle seems to be responsible of a local increase of scalar concentration near the span wise flap ends.

## 1. Introduction

The unsteady aerodynamics and the wake flow generated by idealised flapping wings within a fluid has been studied over many decades in different areas of research, in particular to understand the mechanisms responsible in the propulsion of living beings and in the lift performance of some natural flyers (Ellington et al., 1996). The sustainability of the flight is affected by flow disturbances in the wake of aerodynamic profiles which has been of interest since many years (Gharib and Williams-Stuber, 1989). Many types of forcing strategies have been implemented looking for either an amplification or cancelation of wake disturbances, and mainly focusing on the effect on drag forces (Wu and Shu, 2011). The vortical patterns observed in the wake of an oscillating airfoil (Koochesfahani, 1989) are responsible of the unsteady drag and lift forces and have been related to the complex flight aerodynamics of small natural flyers like some insects. Limited span on wings may lead to an important lift reduction owing to vorticity generated by the edges of the wing, or tip vortices. Experimental studies on the role of tip vortex suppressors have made possible to merge tip vortices with those of the vortex generators thus reducing their unwanted effects on the overall aerodynamics (Heyes and Smith, 2005). When the span of the wing is very limited, the sustained lift of small insect wings is attributed to a stable leading edge vortex which produce

a lift increase by reducing the average top pressure on very high attack angles (Xia and Mohseni, 2013). A considerable theoretical effort have been done to evaluate the contribution of vortices on the global aerodynamic forces over flapping wings (Xia and Mohseni, 2013). It has been recently found that leading edge vortices play an important role on the overall performance of simple flapping wings like a pitching plate (Widmann and Tropea, 2017). Pitching airfoils (Koochesfahani, 1989; Godoy-Diana et al., 2008; Andersen et al., 2017; Negi et al., 2018), plates (Ehrenstein, 2018) and flaps (Wu and Shu, 2011; Vial et al., 2004) at specific frequencies can produce particular alignments of the shed vortices in the wake, triggering drag to thrust transitions accompanied with a considerable increase in the center wake flow velocity. How this transitions, controlled by a simple flapping frequency, may play a role on the transport of a scalar substance injected upstream is an interesting open question. Moreover, beyond the physics on the particular mechanisms involved on the wake properties, we may think in this kind of perturbing techniques as a tool to provide controlled capabilities on the body's surface, vortex shedding and wake thickness as found in airfoil localised surface perturbations (Gharib and Williams-Stuber, 1989) and in recent works on heat transfer enhancement with flexible moving plates (flags) (Gallegos and Sharma, 2017; 2019). The focus of this work is to understand the effect on the wake flow dynamics of a small pitching amplitude trailing edge flap attached to an

---

* Corresponding author.
  *E-mail address:* rohernan@ing.uchile.cl (R.H. Hernández).
  *URL:* http://www.leafnl.uchile.cl (R.H. Hernández).

horizontal flat-plate. As the pitching amplitude of the flap is very small it may be considered as a vibrating surface, making a difference with most of the pitching airfoils mechanisms found in the literature, where finite amplitude pitching motion is the mechanism perturbing the wake (Negi et al., 2018; Godoy-Diana et al., 2008; Andersen et al., 2017; Wu and Shu, 2011). In this work we combine experimental measurements in a wind tunnel with numerical simulations in order to measure and classify the wake response to different pitching frequencies. The flap motion can be considered as an input disturbance originated at the flap's trailing edge which perturbs the wake allowing to probe the frequency response of the wake at low Reynolds numbers. After this wake flow characterisation we extended the numerical simulation solving a scalar transport equation to identify the effect of the unsteady wake on the transport and mixing of a passive scalar.

The structure of the paper is as follows. We describe the experimental and numerical setup in Section 2. The characterisation of the free and forced wake flow is presented in Section 3. Results for the scalar transport under forced oscillations of the wake are presented in Section 4. Conclusions are finally given in Section 5.

## 2. Problem formulation

A schematic diagram of the problem is displayed in Fig. 1. A thin horizontal flat-plate with a trailing edge flap is placed in the test section of the wind tunnel. The plate of length $a$ is at rest and the flap of length $b$ can pitch around an axis passing through the trailing edge of the plate. Thickness of both flat-plate and flap is $e = 1.65$ (mm) where total chord-to-thickness ratio is $L/e \sim 51$ and flap's length-to-thickness ratio is $b/e \sim 20$. In the experimental model the flat-plate has end-plates in order to both keep the plate in place and limit the $z$ plate's span as proposed in (Hernández and Sánchez, 2002). However, in the numerical model we did not use end-plates to allow to understand span end effects on scalar injections.

The numerical simulation solves the mass conservation equation, incompressible Navier-Stokes and scalar concentration equations in primitive variables,

$$\nabla \cdot \overrightarrow{v} = 0 \tag{1}$$

$$\frac{\partial \overrightarrow{v}}{\partial t} + (\overrightarrow{v} \cdot \nabla) \overrightarrow{v} = -\frac{1}{\rho} \nabla p + \nu \nabla^2 \overrightarrow{v} \tag{2}$$
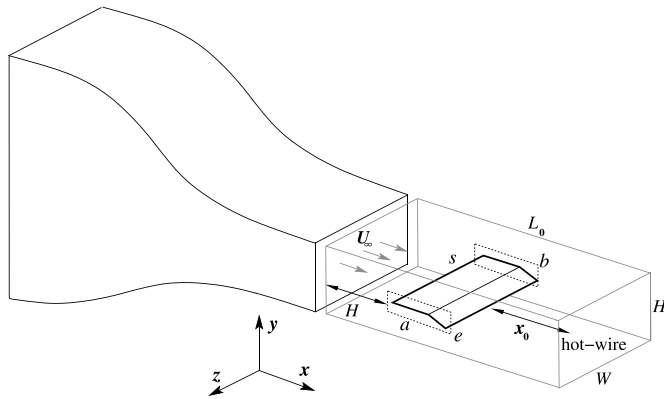


**Fig. 1.** Schematic setup. The experiment was performed in the closed loop wind tunnel of the laboratory in the 2 mt long test section described in detail in (Hernández and Sánchez, 2002; Vial et al., 2004). The portion of the wind tunnel test section (0.2 × 0.2 × 2 m) considered for the numerical simulation domain has height $H = 100$ (mm), width $W = 220$ (mm), length $L_0 = 330$ (mm) Plate and flap dimensions are $a = 54$, $b = 30.4$, total chord $L = a + b$, span $s = 121$ and thickness $e = 1.65$ (mm). In the experiment, the position of the hotwire probe is $x_0$ measured from the flap's trailing edge. End-plates (dashed lines) were used in the experimental set-up. The overall blockage ratio including end-plates is 0.5%.

$$\frac{\partial C}{\partial t} + (\overrightarrow{v} \cdot \nabla) C = \Gamma_c \nabla^2 C \tag{3}$$

Where $\overrightarrow{v} = (u, v, w)$ is the vector velocity, $p$ is the pressure, $\nu$ the kinematic viscosity, $\rho$ is the density, $C(\overrightarrow{x}, t)$ is the scalar concentration and $\Gamma_c$ is the scalar diffusivity. The laminar Reynolds number can be written with the free stream velocity and plate thickness, $Re = U_\infty e/\nu$ as it is the choice in bluff body situations, but it is more appropriate here to write a standard chord-based version $Re = U_\infty L/\nu$.

Velocity disturbances are introduced into the wake flow through the periodic motion of the trailing edge flap. The boundary conditions on the flat-plate surfaces (at rest) are no-slip velocity conditions. However, the boundary conditions on the flap surfaces are determined by an external function which sets an angular flap motion of small amplitude $\alpha_0$ (rd) and frequency $f_0$ Hz. If the pitching flap angle is $\alpha(t) = \alpha_0 \sin(2\pi f_0 t)$ and $\alpha_0$ is small, the trailing edge amplitude may be written as $y(t) = b \sin(\alpha) \sim b\alpha$, where $b$ is the flap length. Therefore, the trailing edge of the flap undergoes a vertical vibrating motion and may be approximated by

$$y(t) = b\,\alpha(t) = A_0 \sin(2\pi f_0 t) \tag{4}$$

In this work, the forcing amplitude $A_0 = b\,\alpha_0$ was kept very small, of the order of a fraction of the flat-plate thickness $A_0 \sim 0.2e$. Such a small amplitude motion of the flap may be considered as a vibrating surface, making a difference with most of the pitching airfoils mechanisms found in the literature, where the boundary layer separation driven by a finite amplitude pitching motion is the mechanism perturbing the wake (Negi et al., 2018; Godoy-Diana et al., 2008; Andersen et al., 2017; Wu and Shu, 2011). Here we try to identify the disturbance amplification taking place in the wake through changes in the excitation (or forcing) frequency $f_0$, a concept which can be found in similar approaches perturbing the wake with the aid of surface strip heaters (Gharib and Williams-Stuber, 1989). The flat-plate wake flow is locally convectively unstable and the spatial evolution of the unsteady dynamics is, to a great extent, determined by both forcing amplitude and frequency (Huerre and Monkewitz, 1990). In the context of wake instabilities, the dimensionless frequency typically invoked is the Strouhal number $S_t$. In the case of bluff bodies like prisms, square and circular cylinders (Jiang et al., 2018) the characteristic length is the cross stream dimension but in the present case it is the flap length $b$, and the Strouhal number reads $S_t = f_0 b/U_\infty$ which in this work is $S_t < 2$ limited by the forcing frequency in the experiments. Dimensionless sampling locations will be refereed either using the plate thickness $x/e$ or using the overall length $x/L$ throughout the text.

### 2.1. Numerical method

The system of equations was solved with the software Fluent (Fluent, 2009) with the built-in control volume formulation with a semi-implicit pressure-velocity coupling algorithm (Patankar, 1980). We adopted a second order spatial discretisation for the pressure and a power law scheme to compute the momentum fluxes. The convergence criteria required that residual of the discretised equations fall below $10^{-5}$ for both the momentum and continuity equations. The time step used was constant $\Delta t = 2.5 \times 10^{-4}$ s, and the number of iterations per time step was variable, being determined by the convergence criteria. The time step is consistently small to ensure stability under the Courant-Levy criterion. The numerical schema exhibits a better behaviour than other methods when convergence in small time steps is required (Jang et al., 1986). In order to resolve high frequency spectral properties of the forced wake, the shedding of Kármán vortices and subsequent motion of the forced cases, the temporal discretisation required time steps under 5 ms. A constant time step size $\Delta t = 2.5 \times 10^{-4}$ s for all the simulations allows to resolve the fundamental mode and higher harmonics at all the forcing frequencies fulfilling the sampling theorem (Polifke and Gentemann, 2004; Middelberg et al., 2004). In the

**Table 1**
Boundary conditions for the Navier Stokes equations in the numerical domain.

| Zone | Coordinates | Boundary condition |
| --- | --- | --- |
| Inlet section | $\vec{x} = (0, y, z)$ | $\vec{v}(\vec{x}, t) = (U_\infty, 0, 0)$ |
| Outlet section | $\vec{x} = (L, y, z)$ | $p(\vec{x}, t) = p_a, \partial_x \vec{v} = 0$ |
| Lateral and top walls | $\vec{x} = (x, \pm H/2, \pm W/2)$ | $\vec{v}(\vec{x}, t) = \vec{0}$ |
| Flat-plate walls | $\vec{x} = (\pm a/2, \pm e/2, \pm s/2)$ | $\vec{v}(\vec{x}, t) = \vec{0}$ |
| Flap walls | $\vec{x} = (0, b, \pm e/2, \pm s/2)$ | $\vec{v}(\vec{x}, t) = \dot{y}(t)\hat{y}$ |

present case, for such a time step $\Delta t$ the sampling frequency is Hz and the corresponding Nyquist frequency is $f_N = f_s/2 = 2000$ Hz. If we associate a wavelength to the Nyquist frequency assuming a mean stream velocity of $U = 1$ (m/s) we get $\lambda = U/f_N = 0.375$ mm, which cannot be resolved in the streamwise coordinate with the mesh spacing we choose $dx \sim 1.65$, $dy \sim 0.33$ mm. But if we consider that in our situation the highest forcing frequency is $f_0 \leq 50$ Hz, it turns out that the sampling theorem is largely fulfilled allowing us to solve wavelengths associated of many higher harmonics of wake flow. Boundary conditions for the simulation are Neumann conditions for the velocity and atmospheric pressure conditions ($p_a$) at the downstream outlet section of the domain (cf. Table 1). On both lateral and top walls (including the flat-plate) we imposed no-slip conditions for all velocity components. The initial concentration of the scalar can be set to any value between $0 \leq C \leq 1$ in any place of the physical domain.

The pitching flap motion is provided by an user defined function written in C programming language, which imparts a periodic motion according to $\alpha(t) = \alpha_0 \sin(2\pi f_0 t)$ where $\alpha_0$ is small. In the present work we will consider a set of three initial conditions for the scalar concentration. (i) In a first case the scalar concentration is set to $C = C_0$ in the lower-half region of the tunnel inlet section. (ii) In a second case the scalar is introduced along the top face of the trailing edge of the flap and finally (iii) in a third case the scalar is introduced into two symmetric strips on the spanwise borders of the flap ends. In all three situations the rest of the domain is set to $C = 0$. The mesh topology of all neighbouring regions of the flat-plate and flap required a fine spatial discretisation, especially the trailing edge of the flap. In the next section we discuss the results of grid tests.

### 2.2. Grid tests

A first set of grid tests were performed to look for grid independent results when the flap is at rest, i.e., the forcing is off. The goal is that the results must be independent of the grid point density and the 3D spatial dimensions of the computational domain. A second necessary check is the accuracy of the fluid velocity solution near the plate in order to provide a comparison of the drag coefficient and boundary layer scaling compared with the classical problem of the flat plate boundary layer in a parallel fluid stream.

Grid tests were focused near the flat-plate and flap where the flow present high velocity gradients. Fig. 2 shows schematically the three-dimensional spatial discretisation for the numerical simulation. Vertical meshing ($y$ axis) consists of two sectors, one equally spaced around the horizontal axis ($\delta y$ constant) followed by a progressively refined linear meshing with constant growth rate, defined as the ratio between successive intervals, $r = \delta y_{i+1}/\delta y_i$, when approaching solid walls.

For each case we recorded the velocity profiles $\vec{v}$ at a laminar and subcritical Reynolds number at different positions downstream the trailing edge of the flap. If we consider a given downstream location $x_0$, for instance at mid span ($x_0, y, 0$), the velocity profiles have three velocity components ($u, v, w$) where, as expected, the $u$ component of the wake is dominant ($|u| \gg |v|, |w|$). A common practice to represent those signals is under the form of time-averaged velocity values at mid span, where the combined effect of the components in the plane ($x - y$) can
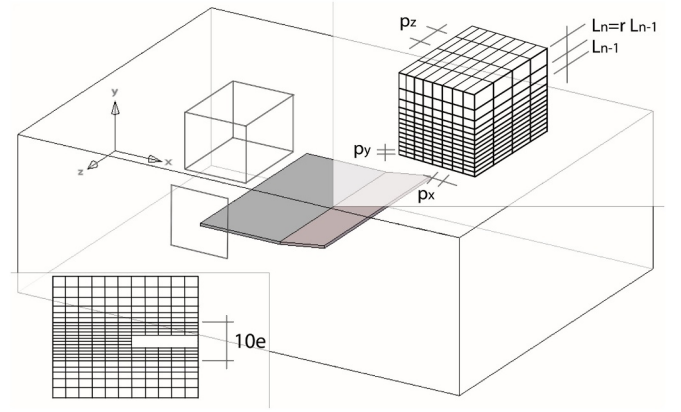


**Fig. 2.** Grid type. Schematics showing the meshing strategy at different zones of the domain. The number of grid points (coarse grid shown) progressively increases near the flat-plate in order to resolve the flat-plate's boundary layer. A linear growth factor $r$ is indicated for each grid type in Table 2. The spatial discretisation in the $k$ coordinate is represented by $p_k = \delta_k$.

be compared later to the experimental velocity data provided by a hotwire anemometer. The resultant velocity profile at given downstream position is written

$$U(y) = \frac{1}{T} \int_0^T (u(x_0, y, 0)^2 + v(x_0, y, 0)^2)^{\frac{1}{2}} dt \tag{5}$$

where $T$ is an appropriate time scale to represent the velocity time history. Fig. 3 display the averaged velocity profiles at different downstream locations $x_0/e = 10, 40$. With high density grids (4 and 5 in Table 2) the profiles begin to collapse, indicating grid independent results in the wake.

The velocity field provided by the numerical simulation allows to calculate several traditional flow parameters like the skin friction coefficient $C_f = \frac{1}{2}(\tau_w/\rho \, U_\infty^2)$ which must be obtained through a standard wall shear calculation, $\tau_w$, evaluating the spatial derivatives of flow velocity at the flat plate walls. The wall shear stress $\tau_w$ is calculated locally at mid span on the flat plate including the flap, and then we compute the skin friction drag by means of a line integral along the chord on one side,

$$D = \frac{s}{L} \int_0^L \tau_w(x, 0) \, dx \tag{6}$$

using the trapezoidal approximation of the numerical integral where $s$ is the plate span. In Table 2 we compare the grid size effect on the drag estimation without forcing the flap by means of the drag coefficient on the entire surface $A = (2 \, s \, L)$ as given by $C_D = (2D)/(\frac{1}{2}\rho A \, U_\infty^2)$. We know that a two dimensional Blasius boundary layer velocity profile provides a reference value to compare with the results of Table 2. The skin friction drag coefficient from a Blasius velocity profile depends on the Reynolds number evaluated at the total chord $L = a + b$ (flat plate and flap) as $C_D = 1.328 \, Re_c^{-\frac{1}{2}}$ (Schlichting, 1968). In Table 2 the resulting drag coefficient is in good agreement with the Blasius's drag coefficient even though the flat plate is of finite thickness $e$. The grid independence test provide an idea of grid sensitiveness and which grid is better when we want to estimate the viscous forces on the plate and therefore the right production of wall vorticity which will finally provide the vortex shedding strength into the wake of the flat plate. In this work grid 5 was our choice as a good compromise between computing time and accuracy.

### 2.3. Experimental setup

The goal of the experiments was to validate the dynamical response of the wake flow to periodic disturbances introduced by the trailing edge flap motion. We performed experimental measurements in the

**Table 2**

Grid sizes for the numerical domain. The growth rate factor $r$ is also indicated. We also indicate the grid size effect on the averaged wall vorticity $\langle\omega_z\rangle_w$ and drag coefficient $C_D$ (total chord $L = a + b$) compared with the Blasius's results (Schlichting, 1968) at $Re_c = 4.3 \times 10^3$.

| Grid | Element size (mm) | | | | N° of elements | Vorticity | Drag | Error |
|---|---|---|---|---|---|---|---|---|
| # | $\delta x$ | $\delta y$ | $\delta z$ | $r$ | $N$ | $\langle\omega_z\rangle_w$ (s$^{-1}$) | $C_D$ | error % |
| 1 | 1.65 | 1.6500 | 3.3 | 1.064 | 459,079 | - | - | - |
| 2 | 1.65 | 0.8250 | 3.3 | 1.082 | 687,666 | - | - | - |
| 3 | 1.65 | 0.5500 | 3.3 | 1.095 | 847,115 | 65.41 | 0.01997 | 1.5 |
| 4 | 1.65 | 0.4125 | 3.3 | 1.098 | 1,029,612 | 66.09 | 0.02034 | 1.4 |
| 5 | 1.65 | 0.3300 | 3.3 | 1.110 | 1,142,965 | 66.13 | 0.02047 | 1.0 |

closed-loop low speed wind tunnel at the LEAF-NL laboratory described in detail in (Hernández and Sánchez, 2002). The wind tunnel has a low turbulence level (defined as the ratio of the rms axial velocity to the average axial velocity) below 0.3% with a very flat velocity profile better than $\pm$ 1% on mean velocity. In this experiment we use a small test section of 20 cm and 2 m long with free stream velocity $U_\infty < 2.0$ ms$^{-1}$. A portion of this relatively small test section (cf. Fig. 1) can be modelled numerically using reasonable grids sizes of Table 2. The flat-plate experimental setup is almost identical to the schematic diagram displayed in Fig. 1. The thin horizontal flat-plate is fixed to the test section with the aid of end-plates (depicted in dashed lines on Fig. 1). The plate and the trailing edge flap are separated by a very

small gap of 0.2 mm where the thickness of both flat-plate and flap is $e = 1.65$ mm. Total chord-to-thickness ratio is $L/e \sim 50$ and flap's chord-to-thickness ratio is $b/e \sim 20$, exactly the same values of the numerical simulation. In this case the flap undergoes a pitching motion achieved by an external B&K 4810 shaker joining the flap ends with a tiny rigid and thin arm system driven directly by the shaker. The flat-plate was mounted between two thin acrylic end-plates sharpened to a knife-edge, which served as support to the wind tunnel walls. The plate span-to-thickness ratio is the same of the numerical simulation, $s/e \sim 73$, which guarantees a two-dimensional flow at low Reynolds numbers (Hernández and Sánchez, 2002; Hernández and Vial, 2008). When the flap is driven by the shaker, its trailing edge can vibrate under harmonic
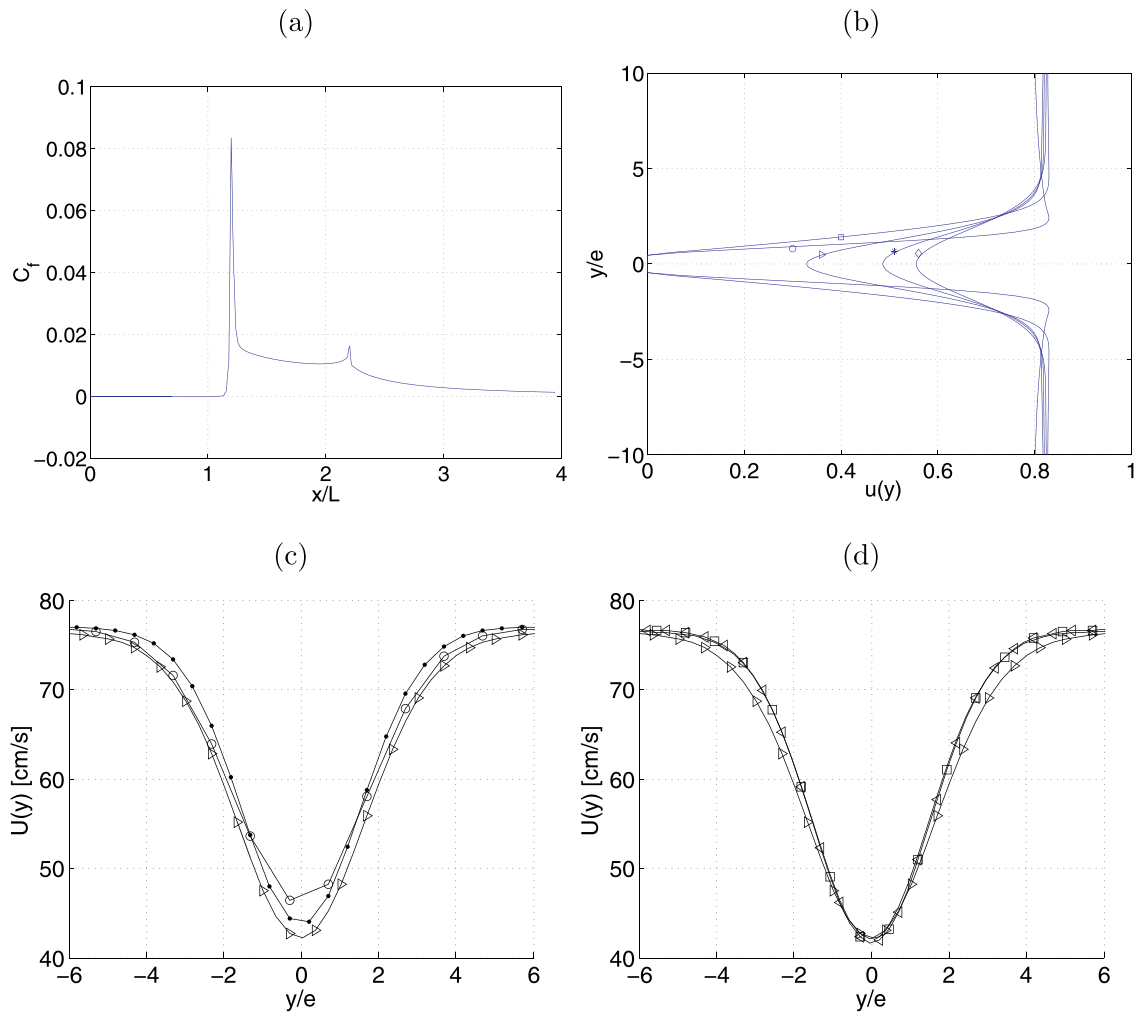


**Fig. 3.** Steady state properties when flap is horizontal at rest at Reynolds number $Re = 4.3 \times 10^3$ (a) Skin friction coefficient at mid span $C_f(x)$ for grid 5. (b) Axial velocity $u(y)$ at different downstream locations $x/L = 1.3, 2.0, 2.6, 3.3, 4$ ($\circ$, $\square$, $\triangleright$, $*$,$\diamond$). (c) Coarser grids $\circ$ grid 1; $\bullet$ grid 2; $\triangleright$ grid 3; (d) Finer grids $\square$ grid 4; $\triangleleft$ grid 5. Position is $x/L = 0.785$ ($x/e = 40$).

forcing according to Eq. 4. A flat (3 dB) frequency response of the flap was obtained for $(0 < f_0 < 50)$ Hz but limited to a small amplitude $(0.1\,e < A_0/e < 0.6\,e)$.

Wake flow velocity was measured with a single probe hotwire anemometer. Wake's velocity profiles were recorded in the near wake at different downstream locations $x/e$ at mid span $(z = 0)$ with a hot film probe (TSI 1201-20). Both probe displacements and forcing parameters were computer controlled through a DT322 Data translation A/D card. The A/D card sampling frequency can go up 250 kHz on a single channel. The minimum sampling frequency for both forced and unforced steady state wake flow velocity signals was 256 Hz. For forcing frequencies $f_0 < 50$ Hz, the sampling frequency was 1024 Hz.

Numerical simulations and experiments were performed with and without forcing at different Reynolds numbers. The velocity profiles along the $y$ axis, $U(y)$, defined by Eq. 5, were measured downstream and were analyzed and compared with experimental results in similar conditions as indicated in Fig. 1.

## 3. Results

In this section we are going to analyse the resulting steady aerodynamics of the wake looking at the velocity profiles recorded downstream the trailing edge of the flap which is here kept horizontal at rest. Under this configuration, the flat-plate and flap produce a simple steady wake flow which is used to calibrate and validate our numerical simulations. The steady wake is considered the base flow where we will introduce velocity perturbations through a small amplitude flap motion or vibration.

### 3.1. Steady wake flow

At relatively low Reynolds numbers the wake flow is steady and linearly stable as there is no evidence of the onset of vortex shedding. The steady wake can be observed in Fig. 4 where we display tri-dimensional contours of spanwise vorticity, $\omega_z$, at $Re = 4.3 \times 10^3$ and the streamwise velocity profiles, $u(y)$, at successive downstream locations starting at the flap's trailing edge. The cross stream velocity component, $v(y)$ was found to be very small, less than 3% the free stream velocity, as the flat-plate is thin enough allowing to place the system below the critical Reynolds number thus without evidence of vortex shedding.

The characteristic properties of the steady wake must be determined before to proceed with the forcing strategy. The steady state wake flow must be stable, within a range of low Reynolds numbers, if we want to consider it as the starting base flow to introduce the external

perturbations.

In the experimental situation, at a given downstream measuring station $x_0$ (for instance at mid span $z = 0$), the wake flow velocity measured with a single hotwire provides an instantaneous measurement of local velocity. In the present experimental conditions the near wake is almost entirely two dimensional along the span, thus the local measure will only reflect the presence of two velocity components $(u, v, 0)$ if the single wire sensor is oriented perpendicular to mean flow with the hotwire axis aligned with the $z$ axis (along flap span). Thus, the effective cooling velocity, i.e. the modulus of the resultant velocity, is what the wire is really sensing, which can be accurately represented by Eq. 5 defined earlier in the text (Comte-Bellot, 1976; Freymouth, 1977).

The two dimensional wake properties were checked out for both the free (and forced wake) from hot wire measurements of the velocity profile at different sampling positions along the span. The near wake flow $(x/e < 100)$ is two-dimensional along 75% of the span, i.e., the velocity profiles differ about 1.5% when compared to the mid-span velocity profile.

Due to the limitations of the hot wire measurements to provide individual velocity components, the velocity profiles from the numerical simulation must therefore be rendered in that form in order to be compared. The measuring station is important because the velocity profile evolves downstream increasing the central velocity while the wake expands in the $y$ direction (cf. Fig. 4). A comparison test between the experimental and numerical velocity profiles has been performed at downstream positions in the near wake, i.e., relatively close to the flap trailing edge. In Fig. 5 we observe an overall good agreement between time averaged velocity profiles in the experiment and the numerical simulation, producing a standard deviation between steady state profiles, less than 8%. Major differences are found in the central low velocity zone $(y \pm e)$ as expected. In experimental cases, the ratio between the minimum velocity and the free stream velocity are close to 0.46, while for simulations, this ratio is slightly higher, reaching a value of 0.51.

The chord/span ratio of the flat-plate is enough to keep the two dimensional flow conditions in both cases. However, as the numerical simulation has no end-plates, the wake structure may be different and possibly influenced by the end effects.

We performed different numerical runs with the finest grid of Table 2 at different Reynolds numbers. Keeping the flap horizontal at rest we have also recorded time series of wake flow velocity at several downstream locations similar to the experimental ones. The systematic increase of the Reynolds number produce a laminar wake flow (without vortex shedding) where the jump between upstream velocity $U_\infty$ and
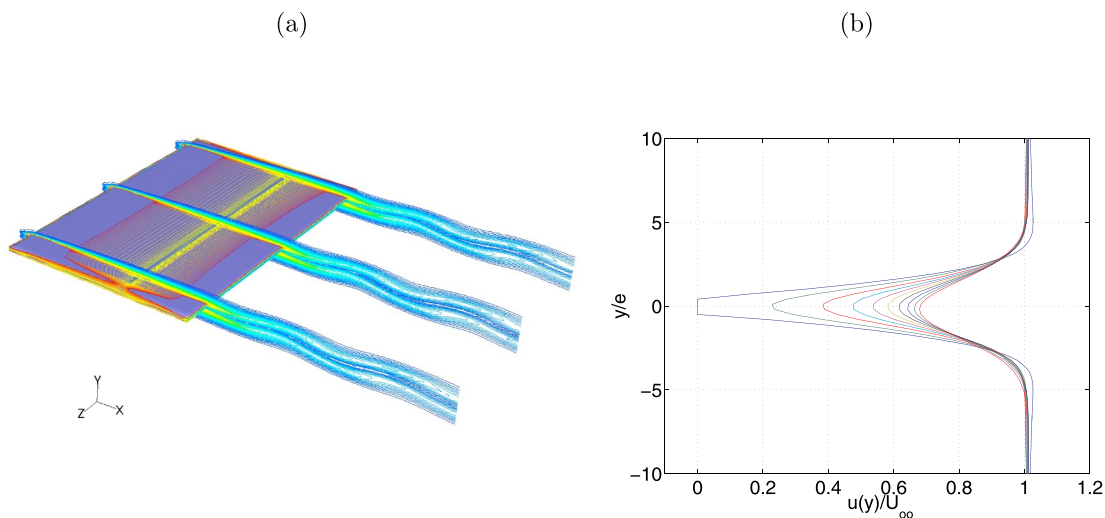
(a)

(b)



**Fig. 4.** Wake flow under steady forcing $(f_0 = 10$ Hz) at $Re = 4.3 \times 10^3$ from the numerical simulation. (a) Contours of spanwise vorticity $|\omega_z|$. (b) Unforced steady state wake. Streamwise velocity profiles $u(y)$ downstream for $(0 \leq x < L)$ at intervals $x/e = 9.5$. The blunt nose profile correspond to the trailing edge position.
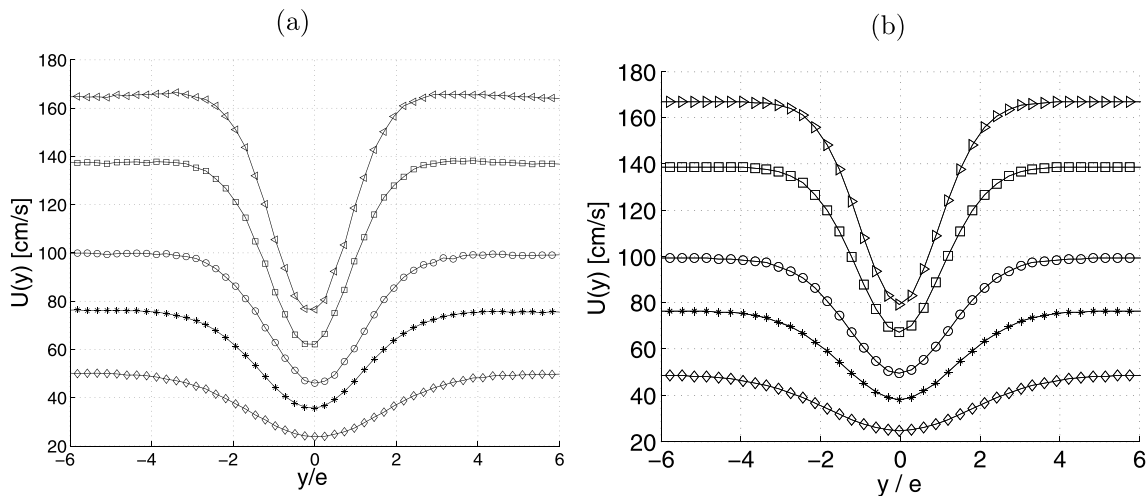
(a)

(b)



**Fig. 5.** Wake velocity profiles at $x/e = 30$ unforced case with the flap horizontally at rest ($f_0 = 0$) at different Reynolds numbers: ⋄, $2.8 \times 10^3$; *, $4.3 \times 10^3$; o, $5.6 \times 10^3$; □, $7.9 \times 10^3$; △, $9.3 \times 10^3$. (a) Experiment (b) Numerical simulation (time $t = 6$ s).

the dead wake velocity ($y \sim 0$) grows with $Re$ as expected (Schlichting, 1968).

The thickness of the flat plate $e$ and the upstream velocity $U_\infty$ are used as the reference quantities to look for a near wake scaling between the steady state velocity profiles of Fig. 5. A comparison between several experimental and numerical velocity profiles is displayed in Fig. 6. We observe good agreement with some differences near the central zone ($y \pm e$) where the lowest flow velocity is found. This small difference decreases as we increase the Reynolds number. For instance, from $Re = 4.3 \times 10^3$ to $Re = 9.3 \times 10^3$ the difference between simulation and experiment drops from 6.3% down to 2.5%. Note that, as we mention before, at the highest $Re$ number tested, the ratio between the minimum speed and the free stream velocity is 0.46 for the experiment, while for simulations is 0.51. These small differences can be attributed to the end-plates used in the experiments to fix the transverse $z$ span of the plate, avoiding the onset of tip vortices typically found in free-end wings (Ringuette et al., 2007; Shyy et al., 2009).

In Fig. 6 we also note how the wake thickness $\Lambda$ decreases with the Reynolds number, as the trailing edge boundary layer thickness does with $Re$. Wake thickness $\Lambda(Re)$ has been estimated at a given downstream location ($x/e = 30$) on the basis of a 1% cutoff between wake velocity and free stream velocity, in order to make a comparison of the resulting scaling. In the literature (see for instance (Schlichting, 1968)) wake thickness is often related to chord-based Reynolds number

making a link with the effects on the upstream boundary layer. In this case we propose a similar procedure usually found on bluff bodies which is based on the boundary layer thickness $\delta$ measured at the trailing edge of the flap. Defining $\Lambda$ approximately as the distance along the $y$ axis between two symmetric points, we compute $|(U(y) - U_\infty)|/U_\infty \le 1\%$ with $U(y)$ the time averaged velocity profile. In Fig. 7 (a) we observe the scaling for $\Lambda(Re)/\delta$ is almost flat when normalised with the boundary layer thickness. In addition, a good collapse of the different velocity profiles is obtained in Fig. 7 (b). Even though the Reynolds range is small, this exercise provides an overall comparison test between the experiments with the numerical simulation.

When the flap is horizontally at rest, the system $y$ symmetry does not allow the production of streamwise vorticity disturbances that may evolve downstream as tip vortices. This may explain why we did not observe tip vortices in the wake flow even with this finite thickness flat-plate at low Reynolds numbers. This situation will change when the flap starts to pitch breaking this flow symmetry.

As the experimental and numerical results show a relatively good agreement, we are pretty confident on the steady wake flow properties and the next step is to investigate the unsteady wake controlled by flap motion. In that case we expect to see the effect of the flap acceleration during the up/down stroke motion on the creation of streamwise vorticity and therefore provide control of the tip vortex production at low Reynolds numbers.
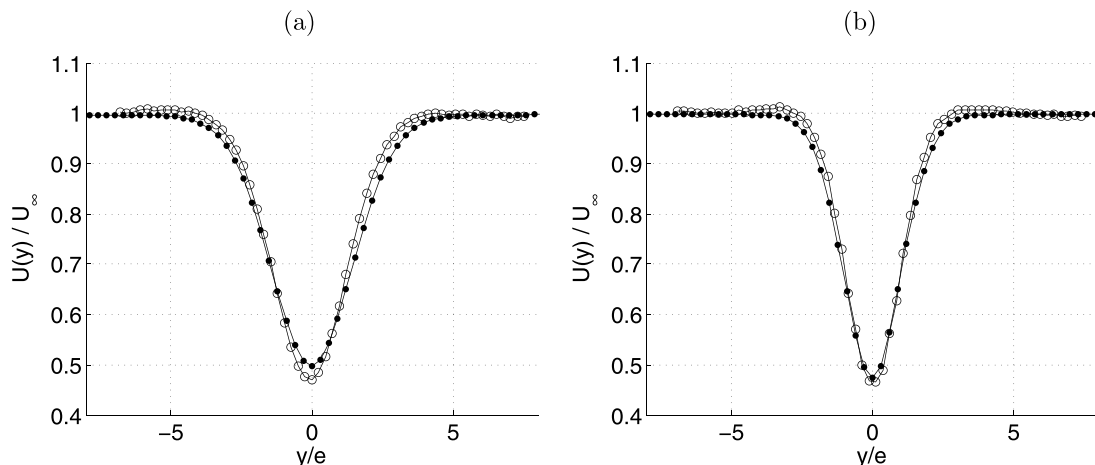
(a)

(b)



**Fig. 6.** Steady state unforced ($f_0 = 0$) velocity profiles with the flap in fixed horizontal position $x/e = 30$ at different Reynolds numbers (o: Experiment; •: Simulation). (a) $Re = 4.3 \times 10^3$. (b) $Re = 9.3 \times 10^3$.
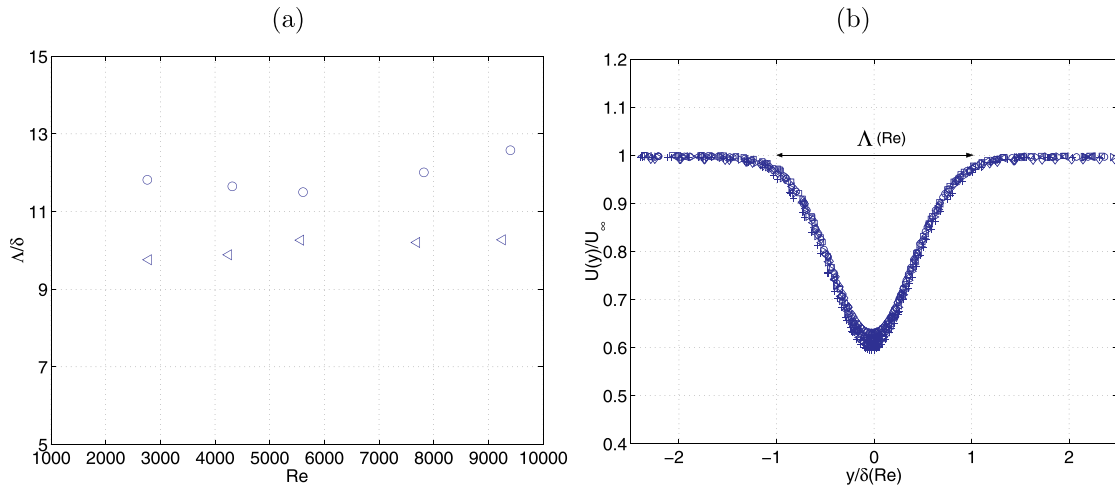
**Fig. 7.** (a) Relationship between wake thickness $\Lambda$ and Reynolds number $Re$ at $x/e = 30$ ($\circ$: Experiment, $\triangleleft$: Simulation). (b) Normalized velocity profiles $U(y)/U_\infty$ at $x/e = 40$, with the flap in fixed horizontal position at $2.5 \times 10^3 < Re < 10^4$ (Numerical simulation).

### 3.2. Forced wake

In this section we focus on the onset of vortex shedding phenomena taking place at particular forcing frequencies dependent on the Reynolds number of the flow (Williamson and Govardhan, 2004). The response of the wake was studied under the periodic forcing of the flap with an externally applied signal (See Eq. 4). Within the range of Reynolds numbers, at a given upstream velocity, the Strouhal number is comprised between ($0.04 < S_t < 2$) which means the forcing frequency is limited between ($2 < f_0 < 50$) Hz and the forcing amplitude used was kept constant $A_0 = 0.2e$.

Once the flap starts to oscillate, the steady wake undergoes a transition from a steady state into a periodic wake flow as shown in Fig. 8. At lower frequencies both wake velocity and vorticity are modulated downstream where the characteristic spatial flow scale is a wavelength $\lambda$ and the imposed time scale is the forcing period $T = f_0^{-1}$. At constant Reynolds number, the higher the frequency $f_0$ the shorter the wavelength $\lambda$ of the wake flow showing the existence of a wake dispersion relationship between frequency $f_0$ and wavelength $\lambda$ of the form $\lambda = U_\infty f_0$. It is interesting to note the effect of the frequency in the transition from a purely oscillating wake (Fig. 8b) into vortex shedding characteristic wake seen in the rest of the slides of Fig. 8. It may be necessary a given level of acceleration of the flap in order to trigger the shedding of individual vortices.

Another interesting effect is that the wake displays a maximum thickness and then shrinks as $f_0$ continue to increase. A similar wake thickness is observed when we compare the steady state unforced case of Fig. 8 (a) with the high frequency forced case $S_t = 1.6$ ($f_0 = 40$ Hz) in Fig. 8 (f). This effect will explain in part, the similarity between mean velocity profiles at both extreme forcing situations (cf. Fig. 11).

A typical flow visualisation of the forced wake flow is shown in Fig. 9 to indicate the similarity with the numerical results of Fig. 8. Even though the Reynolds number is small, the wake development displays the same characteristic features discussed above. The picture was taken at mid span using a smoke tracer introduced upstream and illuminated with a laser light sheet.

The presence of particular frequencies in the wake is provided by the power spectral density (PSD) obtained with the Fourier transform of the $v(t)$ signal, recorded at a given location in the flow. We made use of the standard Fast Fourier Transform (FFT) algorithm (Press et al., 2007). Fig. 10 show typical time history series of cross stream velocity $v(t)$ from the numerical simulation, taken in two different wake locations as well as the corresponding PSD estimation for both the free and forced situation at $S_t = 1$ and $Re = 4.3 \times 10^3$. In the forced case we can identify the fundamental mode ($f_0 = 25$ Hz) as well as two higher harmonics, while in the free steady wake we can not see any characteristic
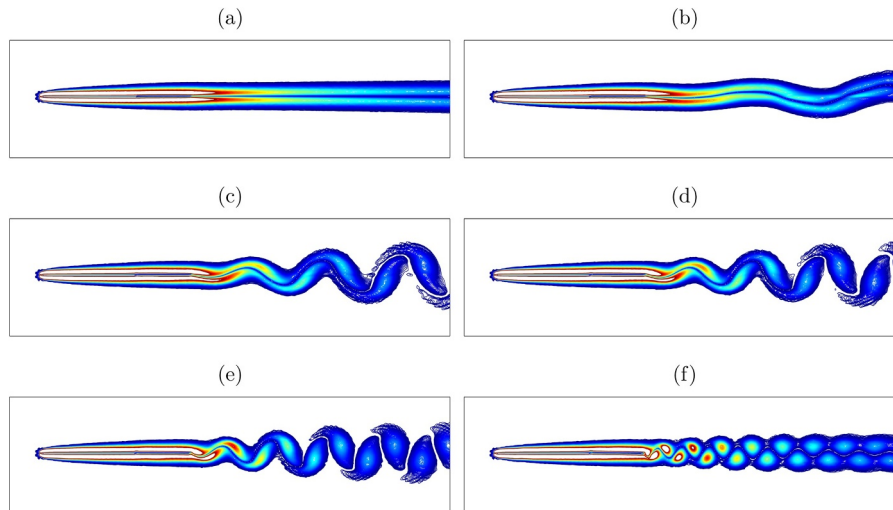


**Fig. 8.** Instantaneous spanwise vorticity fields at the mid-span plane, $0 < |\omega_z| < 200\ s^{-1}$, ($z = 0$) at different forcing frequencies and Reynolds number $Re = 4.3 \times 10^3$ (a) Strouhal number $S_t = 0$. (b) $S_t = 0.4$ (c) $S_t = 0.7$ (d) $S_t = 0.8$ (e) $S_t = 1$ (f) $S_t = 1.6$.
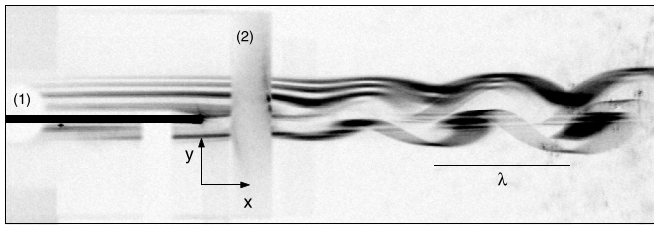
**Fig. 9.** Typical flow visualization of the wake flow from the flat-plate (1) at $s_t = 0.6$ and $Re = 60$. Flow is from left to right. The characteristic wavelength $\lambda$ and the borders of the plexiglass end plates (2) are indicated on the figure.

frequency.

Alternatively, we can see in more detail what would be the effect of the forcing frequency on the wake response in terms of flow velocity profiles with the aid of both time averaged or mean velocity profiles, $U(y)$, as well as velocity fluctuations across the wake under the form of root-mean-square velocity profiles, $U_{rms}(y)$. In order to obtain the velocity profiles, the hotwire probe recorded, at discrete $y$ positions and controlled by a stepper motor, time velocity series long enough to record hundred of forcing cycles. These series were time-averaged producing the characteristic $U(y)$ profiles plotted in Fig. 11 for different frequencies $f_0$. We observe in both cases that wake sensitiveness appears only for a limited range of frequencies, since for very low frequencies and frequencies above 40 Hz ($S_t = 1.6$), the time averaged profile $U(y)$ becomes very similar to the profile of the free wake without forcing (plotted in continuous line).

In both cases there are two resonant frequencies, hereafter denoted by $f_n$ associated to a narrow wake and $f_w$ associated to wider wake ($f_n < f_w$) producing a very different wake topology. At $f_n$ the wake width shrinks as the alignment of the vortex structures occurs near the centerline of the wake, in agreement with the observations of (Koochesfahani, 1989; Andersen et al., 2017). If we increase the forcing frequency reaching $f_w$ the wake increases its center velocity (the velocity profile becomes flatter) and, at the same time, the spatial thickness of the velocity profile increases remarkably as the vortices are shed at the maximum stroke during the forcing cycle (Hernández and Vial, 2008). For the experimental case this frequency gives a Strouhal number $S_t = f_w b/U_\infty = 1$, while for simulations it is slightly lower, $S_t = 0.8$, at the same Reynolds number, a difference attributed (probably) to the onset of tip vortices in the idealised numerical situation without end-plates.

Fig. 12 show the normalised velocity fluctuations as a function of forcing frequency under the form of *rms* velocity fluctuation profiles $U$

$(y)_{rms}$ at $Re = 4.3 \times 10^3$ defined as,

$$U(y)_{rms} = \left( \frac{1}{T} \int_0^T u'(y, t)^2 \, dt \right)^{\frac{1}{2}}$$

Where $u'(y, t) = (U(y, t) - U(y))$ represent instantaneous velocity fluctuations and $U(y)$ represents the time averaged velocity profile over almost $t = 30$ s. We identify two symmetrical maxima with respect to the $y$ axis, for each frequency. They represent the location where the modulated wake vorticity reaches maximum fluctuations produced either from wake undulations (at low frequencies) or vortex shedding (at higher frequencies) as it is shown in Fig. 8. Lateral wake expansion takes place when their position move away from the plate for a given frequency. Nevertheless, the maximum wake expansion observed is modest ($y/e \sim \pm 4$ at $f_0 = f_w$) as compared with the one-thickness ($y/e \sim \pm 1$) or narrow wake observed at low frequencies at $f_0 = f_n$. A good agreement is observed between the experimental and the numerical results regarding both relative amplitude and location on the $y$ axis.

The downstream velocity fluctuations profiles of Fig. 12 are connected to the sweep cycle of the velocity profile at the trailing edge of the flap. In Fig. 13 we observe the symmetric initial expansion of the axial velocity profile during one forcing cycle. The small amplitude motion of the rear solid edge of the flap (zero velocity) is indicated with a double arrow. When the cycle is completed the velocity profile executes a symmetric swept producing the observed wake expansion early discussed here. A notorious difference of the averaged downstream velocity profiles is found when compared with the equivalent profile in the unforced situation in Fig. 4.

Beyond the evident changes of the wake properties, we may think in this perturbations as a mechanism to control the wake thickness through a single parameter, the forcing frequency; A rapid change of $f_0$ may allow us to switch from an intense and narrow wake at $f_n$ to an expanded and less intense wake at $f_w$ and vice versa, providing controlled capabilities on the flap surface, vortex shedding and wake thickness which by the way is perhaps closely related to fields like heat transfer enhancement (Gallegos and Sharma, 2017), and localised surface perturbations on airfoils (Gharib and Williams-Stuber, 1989).

The role of the forcing frequency on the wake controlled expansion can be summarised looking into the behaviour of an integral quantity as the kinetic energy of the wake. We can invoke the kinetic energy associated to flow fluctuations splitting the fluid velocity as a mean velocity profile $U(y)$ and fluctuations $u'(y, t)$ allows to write $U(y, t) = U(y) + u'(y, t)$. An approximation of the kinetic energy is $E_k = \frac{1}{2}(U^2(y) + 2U(y)u'(y, t) + u'^2(y, t))$. If this equation is time-
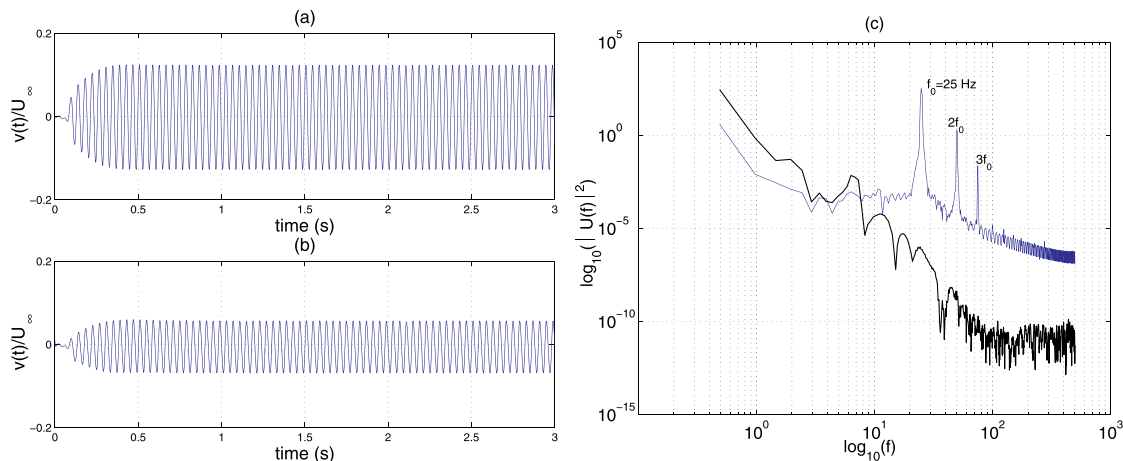


**Fig. 10.** Forced wake time velocity series at $S_t = 1$, $A_0 = 0.2e$ and $Re = 4.3 \times 10^3$. Time history of velocity component $v(t)$ from the numerical simulation at two downstream locations. (a) Sampling point $(x, y) = (40e, 0)$ and (b) Sampling point $(x, y) = (40e, 4e)$ and (c) Power spectral density of the forced wake at $(x, y) = (40e, 4e)$. The lower curve corresponds to the power spectral density when the forcing in turned off.
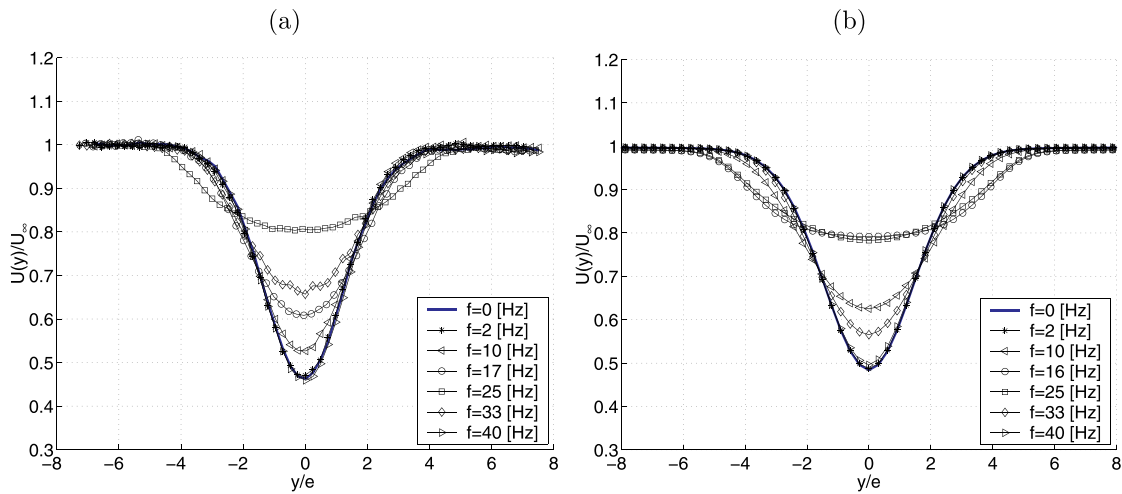
**Fig. 11.** Time-averaged velocity profiles $U(y)$ at Reynolds number $Re = 4.3 \times 10^3$ for different forcing frequencies. (a) Experimental results: (*) $S_t = 0.08$; (•) $S_t = 0.4$; (◦) $S_t = 0.7$; ( ☐ ) $S_t = 1$; (◁) $S_t = 1.3$; (▷) $S_t = 1.6$, free wake in continuous blue line. (b) Numerical results: (*) $S_t = 0.08$; (•) $S_t = 0.4$; (◦) $S_t = 0.65$; ( ☐ ) $S_t = 1$; (◁) $S_t = 1.3$; (▷) $S_t = 1.6$. (For interpretation of the references to colour in this figure legend, the reader is referred to the web version of this article.)
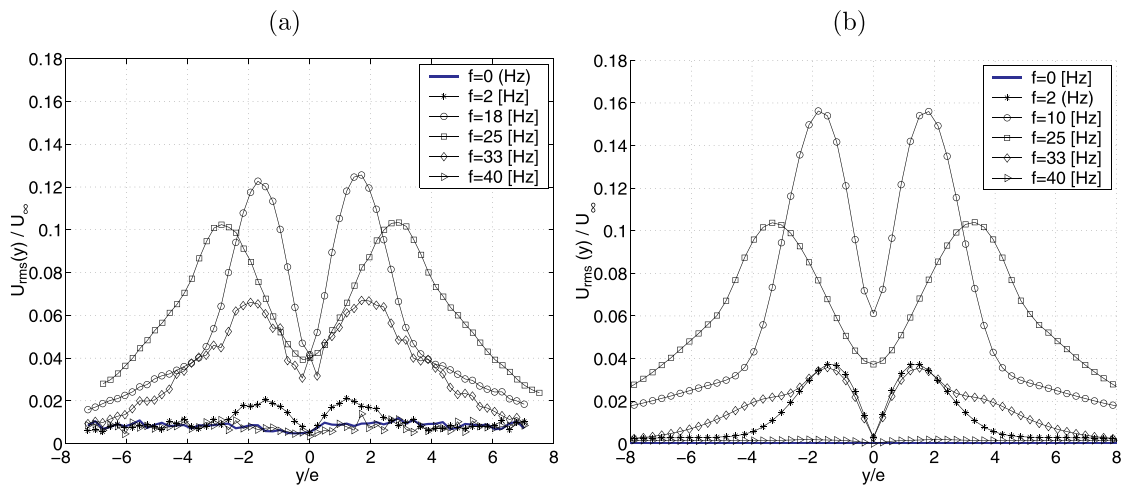


**Fig. 12.** Velocity fluctuation profiles $U(y)_{rms}/U_\infty$ at Reynolds number $Re = 4.3 \times 10^3$. (a) Experiment: (*) $S_t = 0.08$; (o) $S_t = 0.7$; ( ☐ ) $S_t = 1$; (◁) $S_t = 1.3$; (▷) $S_t = 1.6$ (b) Numerical simulation: (*) $S_t = 0.08$; (o) $S_t = 0.4$; ( ☐ ) $S_t = 1$; (◁) $S_t = 1.3$; (▷) $S_t = 1.6$.
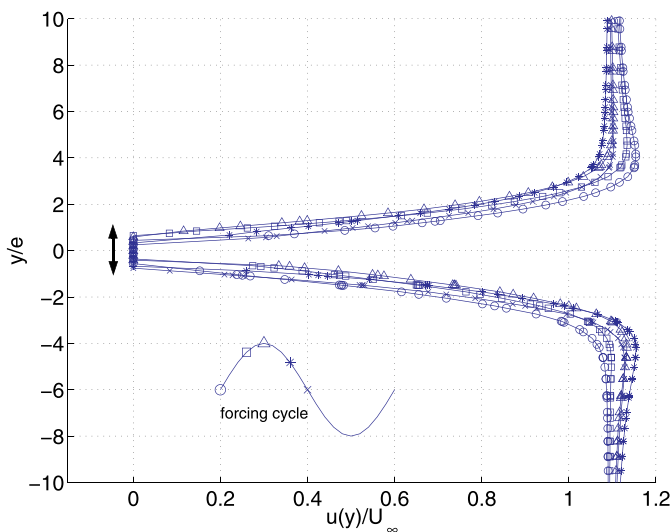


**Fig. 13.** Comparison of the velocity profile at the trailing edge of the flap during a single forcing cycle $S_t = 0.4$ and $Re = 4.3 \times 10^3$.

averaged ($\langle \rangle$) the last term represents the kinetic energy of flow fluctuations $\langle u'^2 \rangle$ which will help us to display the effect of forcing frequency across the wake in terms of kinetic energy fluctuations.

In Fig. 14 (a,b) we plot the contours of the energy fluctuations $\langle u'^2(y) \rangle$ as a function of forcing frequency and cross stream coordinate $y$. Time averages of 30 s where performed in the experiment and 10 s during the numerical simulation. The two dimensional plot represents the frequency response of the flat-plate as a spatial distribution of kinetic energy fluctuations. The narrow wake occurs as a red spot of high energy fluctuations close to $y/e \sim 1$ and the expanded wake occurs at higher frequencies with less intense energy fluctuations. As we mentioned before the two characteristic forcing frequencies, $f_n$, $f_w$ may be used as a control parameter to perform wake contractions/expansions and eventually allowing to modify the shear stress on the flap surfaces as the overall forces on a streamlined body (a flat plate) are related to wake thickness (Schlichting, 1968).

The spectral content of the narrow wake fluctuations at frequency $f_n$ is compared to the steady wake when forcing is turned off in Fig. 14 (c) and (d). Similar to Fig. 10, we considered here the power spectral density (PSD) of the wake streamwise velocity, $u(t)$. The spectral components of the wake at $S_t = 0.7$ ($f_0 = 17$ Hz) and $Re = 4.3 \times 10^3$ clearly display the fundamental frequency $f_0$ and again similar higher harmonics distribution in both cases. The unforced steady wake is the
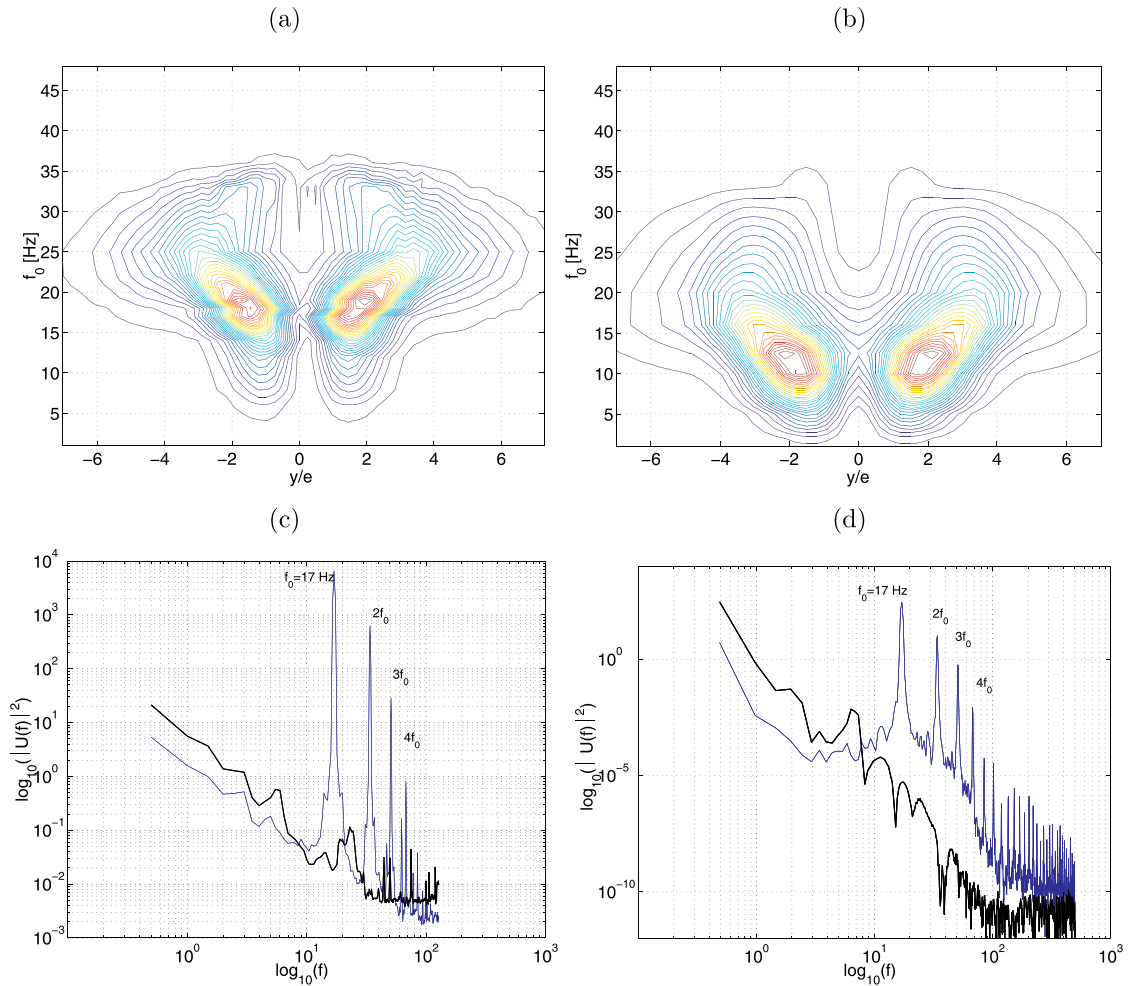
**Fig. 14.** Contour of isovelocity fluctuations as a function of forcing frequency $f_0$ and $y$ coordinate at Reynolds number $Re = 4.3 \times 10^3$. (a) Experiment with Nyquist frequency 256 Hz (b) Numerical simulation with Nyquist frequency 512 Hz. Comparison of power spectral density (PSD) of time velocity series downstream at $Re = 4.3 \times 10^3$ and $x/e = 40$. We display both the forced wake PSD at $S_t = 0.7$ (blue) and the free wake without forcing (black) at the same Reynolds number. (a) Experiment (b) Numerical simulation. (For interpretation of the references to colour in this figure legend, the reader is referred to the web version of this article.)

base solution on which we add the flap forcing, and if we wish to perform a fine tuning of the wake's spectral content we have to change the wake amplification through the Strouhal number. This effect is remarkably achieved with a very small flap displacement provided that the frequency be tuned in the right value. As the velocity of the flap increases linearly with the forcing frequency, as it does the time derivative of Eq. 4, the energy input into the wake may be important as well as the forces on the flat plate but specially on the moving flap.

If the wake shrinks or expands, the drag over the body will change accordingly, as the drag is directly related to the far downstream velocity profile thickness invoking the momentum theorem (Godoy-Diana et al., 2008). We will consider the wall shear stress integrated on the flap surface to be an estimation of the drag and unveil its relationship with the flap's upward/downward motion and determine the influence of the Strouhal number.

This effect can be seen in Fig. 15 (a) where we display the averaged shear stress in the flow direction on the top flap wall (at mid span) during a single forcing cycle. The averaged shear stress at mid span is given by

$$\langle \tau_w \rangle = \frac{1}{b} \int_0^b \tau_w \, dx$$

A single flap forcing cycle is represented on the lower part of Fig. 15 (a). As the flap amplitude is small, the average shear stress represents mainly the drag on the flap surface and for the range of Strouhal

numbers here considered, there is a progressive evolution of the shear stress cycle with the Strouhal number.

The four curves of Fig. 15 were normalised by $\tau_{w0}$ the averaged mid-span shear stress on the flap without forcing. A similar amplitude span is observed during one forcing period, with the same initial value. We distinguish a progressive evolution of the average shear stress cycle, going from low frequencies $f_n$ ($S_t = 0.4$) to higher frequencies $f_w$ ($S_t = 0.8$). As the relative starting phase of the flap motion is the same for all cases, the relative drag cycle time scale $T_d$ may or not match the forcing period $T$. In Fig. 15 b) the relative drag cycle $T_d/T$ increases with the Strouhal number. Neither the narrow nor the wider wake condition match the forcing cycle, only an intermediate forcing condition allows to complete the forcing cycle in one forcing period, $S_t = 0.6$. This synchronisation has an effect on the total drag experienced by the entire system which must be computed during a forcing cycle.

The total frictional force (per unit length) on the flap can be estimated as

$$D = \rho \, s \int_0^b \tau_w \, dx$$

Then we calculate the mean drag over one forcing period as

$$\langle D \rangle = \frac{1}{T} \int_0^T D(t) \, dt$$

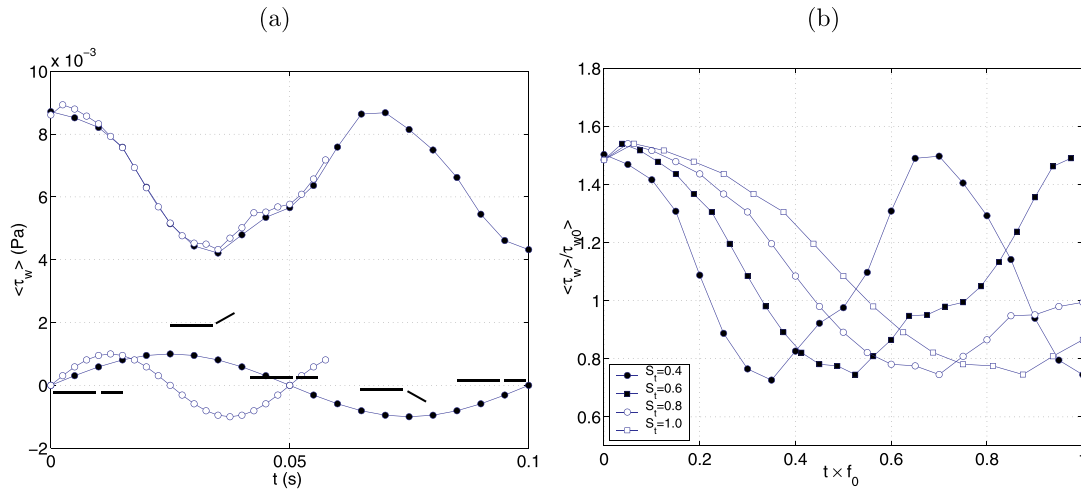The mean drag over the flap is displayed in Table 3 presenting an

(a)                                                                 (b)



**Fig. 15.** (a) Averaged shear stress $\langle \tau_w \rangle$ over the top wall of the flap during one forcing cycle. (•) $S_t = 0.4$ ($f_0 = 10$ Hz); (○) $S_t = 0.8$ ($f_0 = 20$ Hz). The flap cycle is indicated over the forcing signal during one period for $St = 0.4$ ((•) curves below). (b) Normalized averaged shear stress $\langle \tau_w \rangle / \tau_{w0}$ at the top wall of the flap during one forcing cycle. We considered $\tau_{w0}$ the wall averaged shear stress when the system is in steady state without forcing. Each curve represent a different Strouhal number $S_t = 0.4, 0.6, 0.8, 1.0$. Both figures were taken at Reynolds number of $Re = 4.3 \times 10^3$.

excess of about 10% with respect the steady state drag of the unforced case.

This comparison between numerical and experimental results confirm a similar wake receptivity o frequency response. The order of magnitude of the resonant frequencies $f_n, f_w$ is similar but slightly lower in the numerical case. This difference may be originated from the fact that the experiment was performed with end-plates, thus suppressing the onset of streamwise vorticity $\vec{\omega}_\perp = (\omega_x, \omega_y)$ near the flap ends during its motion. If we could remove the end-plates in the experiment, the flap accelerations would produce additional $\omega_\perp$ vorticity in the form of tip vortices. Adding end-plates into the numerical simulation will suppress tip vortices, un unwanted effect in the following section.

In what follows, we will show the effect of the unsteady wake on the transport and mixing of a scalar substance injected upstream in the system and we unveil the presence of tip vortices using the scalar as a tracer.

## 4. Passive scalar transport

In this section we will study the interaction of a passive scalar substance with the unsteady wake flow of the flat-plate at forcing frequencies $f_n$ and $f_w$. Carbon monoxide ($CO$) was considered as a passive scalar substance to determine both cross stream ($y$) and streamwise ($x$) transport dynamical properties. Carbon Monoxide standard properties are density $\rho = 1.1233$ (kg m$^{-3}$), kinematic viscosity $\nu = 1.7500 \times 10^{-5}$ (m$^2$ s$^{-1}$), and molecular diffusivity $\Gamma_c = 2.88 \times 10^{-5}$ (m$^2$ s$^{-1}$). We have chosen $CO$ as a passive scalar since it is one of the gases with similar density (and viscosity) with air under same atmospheric conditions. The Schmidt number of the mixture is defined as $S_c = \nu/\Gamma_c = 0.54$ which indicates an important diffusive effect during the downstream transport of the scalar. When diffusivity of solute in the solvent is low and the kinematic viscosity ($\nu$) is high, the Schmidt number is high and the solute dynamics makes mixing very difficult under laminar flow

conditions. On the contrary, when the Schmidt number is small, $Sc < 1$, both substances will tend to mix easily by diffusive mechanisms. In this configuration the numerical simulations will provide complementary data to the experimental test on the transport properties of the forced wake.

### 4.1. Scalar distributions

In order to understand the ability of the wake to transport a particular distribution of a scalar substance, we have considered three different initial scalar distributions. The idea is to identify how the wake mix the scalar downstream and how the forcing may affect the scalar distribution. First we attain a steady (unforced, $f_0 = 0$ Hz) wake flow regime as the starting flow condition for the scalar injection. After this condition is reached, at a given time, we activate the scalar injection at the same time we turn on the flap motion. In the three situations the forcing frequencies we choose are $f_0 = f_n, f_w$ corresponding to the maximum values of energy fluctuations found on Fig. 14, and responsible of the narrow and wide wake states respectively.

#### 4.1.1. Case 1: Half inlet scalar injection

In this first case, we fill up the lower half of the numerical domain with the scalar, which is continuously injected at the inlet upstream (cf. Fig. 16). Then we proceed to move the flap at $f_n$ ($S_t = 0.4$) and then at $f_w$ ($S_t = 0.8$), keeping the Reynolds number at $Re = 4.3 \times 10^3$. Fig. 17 give us an idea of the effect of the forced wake on the passive scalar
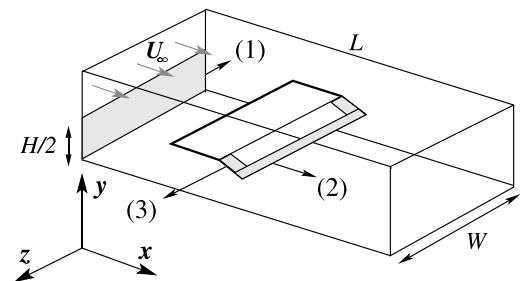


**Fig. 16.** (1) Case 1. Scalar is uniformly injected in the lower half of the inlet section. (2) Case 2. Scalar is uniformly injected on the top strip at the trailing edge of the flap (strip distribution width $\Delta x/e = 3$) (3) Case 3. Scalar is uniformly injected on two strips located symmetrically on top side of the flap (strip width $\Delta z/e = 3.5$).
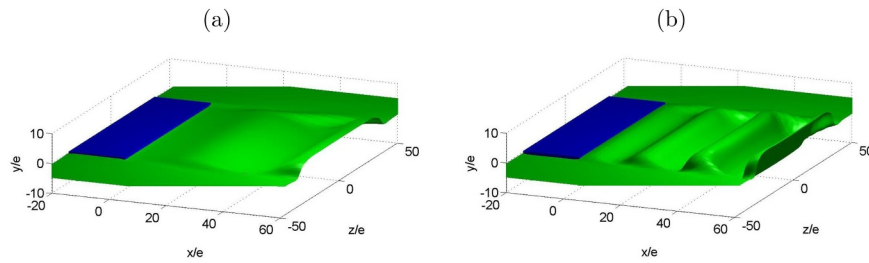
**Table 3**
Drag over the flap as a function of Strouhal number. $\langle D \rangle$ is the mean drag by integration of wall shear stress over the entire flap surface during one forcing cycle. We considered $D_0$ the total drag over the unforced horizontal flap when the system is in steady state. The Reynolds number is $Re = 4.3 \times 10^3$.

| $S_t = f_0 b/U_\infty$ | 0.4 | 0.6 | 0.8 | 1.0 |
|---|---|---|---|---|
| $\langle D \rangle/D_0$ | 1.098 | 1.108 | 1.117 | 1.114 |

**Fig. 17.** Wake visualisation in case 1. Distribution of scalar concentration $C = 0.5$ (green) at $0.4T$ with $T = 1/f_0$ and $Re = 4.3 \times 10^3$. (a) Case 1 at $S_t = 0.4$. (b) Case 1 at $S_t = 0.8$ (flap in blue). (For interpretation of the references to colour in this figure legend, the reader is referred to the web version of this article.)

distribution at forcing frequencies $f_n$, $f_w$. The air-scalar interface follow the wake oscillations displaying the same characteristic wavelength $\lambda$ observed for in the downstream $\omega_z$ vorticity pattern.

In such a situation, we may ask if the oscillating wake can enhance or act as a barrier for the transport of the scalar from the lower half region into the upper half region. This is a practical property found on air curtains created by air-jets intended to isolate dangerous scalars like smoke and temperature in tunnel fires (Lecaros et al., 2010).

First we studied the evolution of the concentration profiles of the passive scalar across the transverse coordinate $y$ for both frequencies. Fig. 18 show the instantaneous, averaged and *rms* concentration profiles at a distance of $x/e = 30$. In Fig. 18 (a,b) we observe the influence of the forcing duty cycle in both cases through the onset of inflexion points in the corresponding profiles as a function of the time (forcing

period $T = f_0^{-1}$). This effect indicates an alternating scalar transport across the wake. The way the scalar concentration change from the lower side of the wake ($C = 1$ at $y/e < 0$) into the upper part ($C \rightarrow 0$ at $y/e > 0$) is being clearly influenced by the forced response of the wake. The characteristic cross stream extension of the concentration at the middle of the wake, i.e., near $y/e = 0$, is greatly increased when we place the wake under a resonant condition setting $S_t = 0.4$ and then $S_t = 0.8$ (cf. Fig. 12). The growth of the characteristic thickness $\Delta$ can also be seen in Fig. 18 d) where the effect results in a wider *rms* spatial distribution, which may be considered as a wide interface around $C = 0.5$, increasing the scalar transport on the $y$ direction across the wake. Fig. 18 c) displays the effect of the forcing frequency on the averaged concentration profiles, where we observe a net cross scalar flow from the lower side (or contaminated) into the upper side (cleaner)
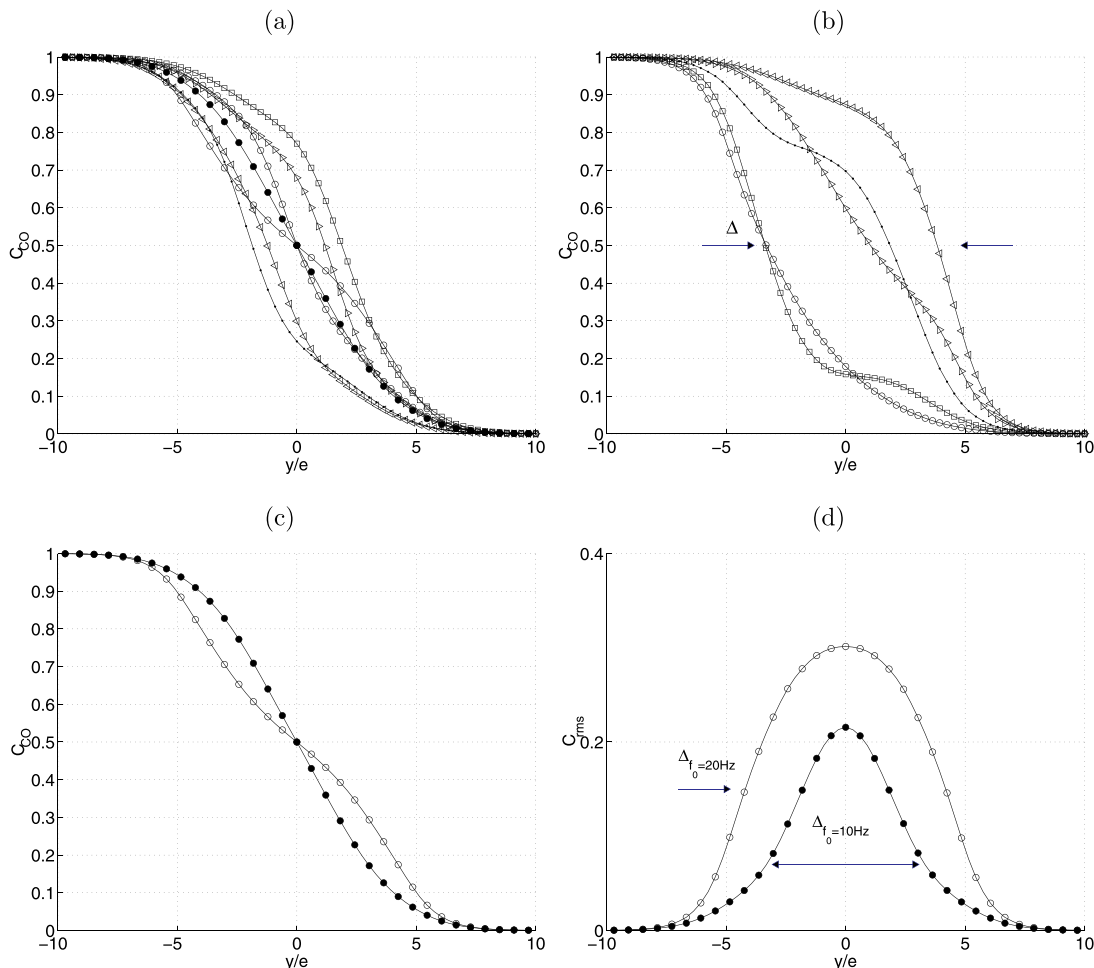


**Fig. 18.** Case 1. Concentration profiles $C(y)$ at $x/e = 30$ as a function of forcing duty cycle, (•: 0.2T; ∘: 0.4T; □: 0.6T; ▷: 0.8T; ◁: 1T) at Reynolds number $Re = 4.3 \times 10^3$. (a) $S_t = 0.4$. (b) $S_t = 0.8$. (c) Mean and (d) *rms* concentration profiles versus $y$. (•: $S_t = 0.4$; ∘: $S_t = 0.8$).

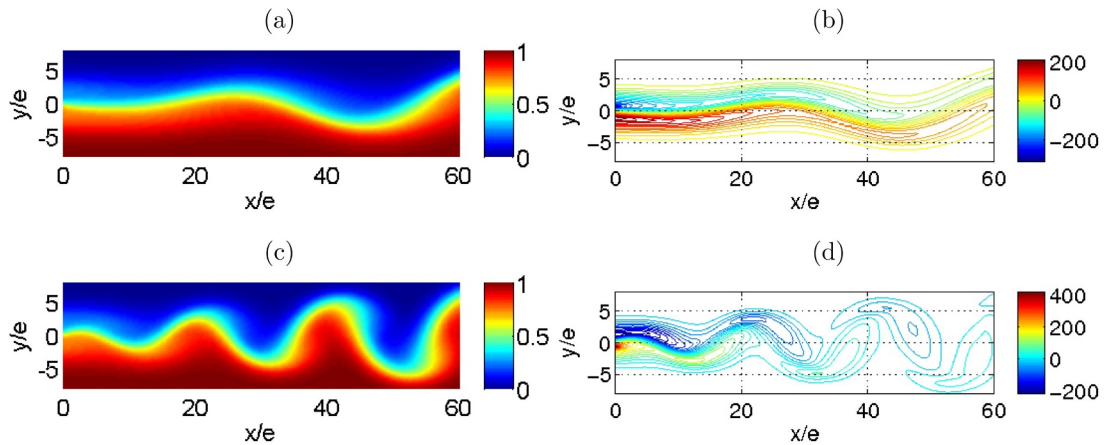**Fig. 19.** Case 1. Instantaneous isoconcentration ($C$) and isovorticity fields ($\omega_z$) at mid span $xy$-plane ($z = 0$) at Reynolds number $Re = 4.3 \times 10^3$. (a) Iso-concentration at $S_t = 0.4$ and simulation time $t = 7.4$ (s). (b) Iso-vorticity at $S_t = 0.4$, $t = 7.4$ (s). (c) Iso-concentration at $S_t = 0.8$, $t = 6.6$ (s). (d) Iso-vorticity at $S_t = 0.8$, $t = 6.6$ (s).

of the wake.

If we look at the middle region of the wake ($y = 0$) in Fig. 18 c) the averaged scalar concentration is the same independent of the forcing frequency. However, in the middle wake the *rms* profiles are quite different both in characteristic thickness $\Delta$ and amplitude as the Strouhal number increases from $S_t = 0.4$ to $S_t = 0.8$. In order to understand the downstream evolution of the scalar distribution we plot the scalar substance in $xy$ planes starting from the flap's trailing edge. Fig. 19 shows the isoconcentration contours at $S_t = 0.4$, 0.8. The wavelength $\lambda$ associated with the oscillation of the wake vorticity is also found here on the scalar concentration contours. The higher the oscillation frequency, the lower the associated wavelength. When $S_t = 0.4$ the wavelength $\lambda/e \sim 35$ ($\lambda/b \sim 2$), while for $S_t = 0.8$ we have $\lambda/e \sim 20$ ($\lambda/b \sim 1$). As we can see, the wavelength $\lambda$ of the oscillating wake can be varied according to the dispersion relation $\lambda = U_\infty/f_0$ (Hernández and Sánchez, 2002). On the other hand, at $S_t = 0.8$ the wake is widest and oscillates at a wavelength very close to the flap length $\lambda \sim b$. This result agrees with previous results (Hernández and Vial, 2008; Koochesfahani, 1989), when $f_0 = f_w$ the Strouhal number based on the moving flap $S_t \sim 1$. On a practical point of view, that means we can tune in the wavelength of the flow and determine the vorticity content at each forcing frequency. Fig. 19 shows isovorticity contours at $S_t = 0.4$, 0.8 in the mid-span $xy$-plane at Reynolds number $Re = 4.3 \times 10^3$. We observe a continuous downstream advection of spanwise vorticity decreasing progressively as moving downstream. Note the difference in wake thickness across the $y$ direction in both cases.

In the snapshots of Fig. 19 we observe a spatial similarity between both the scalar distribution and the vorticity structure of the wake. We did not find a phase lag between both unsteady fields. The scalar unsteadiness follows the wake vorticity and makes the air-scalar interface to evolve downstream in phase (fluctuates coherently) with the wake vorticity. This effect has been observed for the entire range of Strouhal

number. If we consider the spatio-temporal modulation of the air-scalar interface we observe zones of high concentration protruding into the upper lower concentration zones, resulting in a local increase of the scalar mass flow into the upper region. This effect is enhanced as frequency increases as it can be seen on Fig. 19 (a,c) and should be responsible of the net increase of scalar transport in the cross stream direction, which is considered an unwanted effect in some practical situations like in scalar confinement technologies (Lecaros et al., 2010). In the present case the downstream scalar advection by wake vorticity is a dominant transport mechanism. However, we may use the frequency as a control parameter to fine tuning cross stream scalar fluxes indirectly by the choice of vorticity structure. This can be inferred in the plots of Fig. 18 (d), where *rms* concentration profile across the $y$ coordinate becomes narrower at $f_n$ forcing frequency and wider at $f_w$ frequency. This effect is not clear on the averaged concentration profiles.

It seems that the oscillating wake has a (limited) potential capacity to enhance cross stream scalar transport from the lower ($y < 0$) to the upper ($y > 0$) wake domain, as it was intended to show in this particular injection case, where frequency $f_0$ and wavelength $\lambda$ appear to be the control parameters interconnected by its dispersion relationship.

### 4.1.2. Case 2: Trailing edge scalar injection

In this second case the passive scalar substance injection occurs at the trailing edge of the flap (cf. Fig. 16 b) by setting the concentration of $C = 1$ on the last 5 (mm) of the flap trailing edge ($\Delta x/e = 0.3$) on the upper flap surface. The idea was to inject the scalar close to the zone of spanwise vortex shedding, as it is typically used in some passive scalar tracer in flow visualization methods. The initial flow condition and forcing frequencies considered here are the same used in the first case ($S_t = 0.4$, 0.8 and $Re = 4.3 \times 10^3$). Fig. 20 displays a three-dimensional visualization of the distribution of passive scalar substance observed in the wake at $S_t = 0.4$, 0.8. The injection of the passive scalar substance is
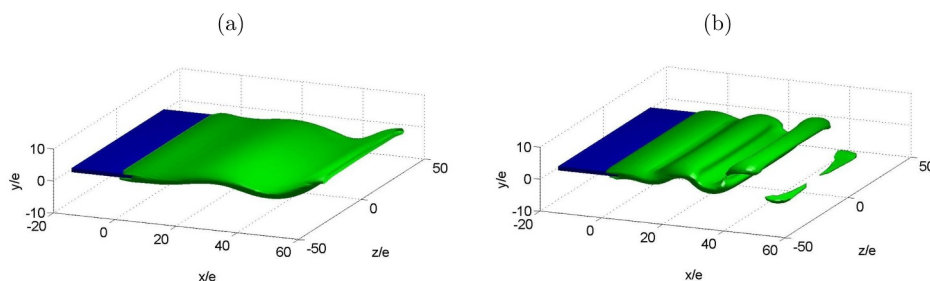


**Fig. 20.** Wake visualization in case 2 (flap in blue). Distribution of scalar $C = 0.05$ at $t = 0.4T$ where $T = 1/f_0$ at $Re = 4.3 \times 10^3$. (a) $S_t = 0.4$. (b) $S_t = 0.8$. (For interpretation of the references to colour in this figure legend, the reader is referred to the web version of this article.)

being performed continuously in the edge of the flap and transported downstream. To answer the question on how effective are both forced flow situations (frequencies $f_n$, $f_w$) in the scalar transport ? we take a look into Fig. 21 where we show the concentration profiles downstream at $x/e = 30$. When $S_t = 0.4$, the profiles have a bell-like distribution, which moves on the $y$ axis depending on the forcing duty cycle. Maximum concentration of the scalar was found between $\pm\ 2e$. While for $S_t = 0.8$ the maximum concentration tends to be located between $\pm\ 3.5e$. The location for the maximum concentration tends to be influenced by the velocity fluctuations already observed in Fig. 12, where local maxima of velocity fluctuations occur in similar positions. At $S_t = 0.8$ the scalar distribution across $y$ axis also reaches its widest $y$ extension. Time averaged and *rms* concentration profiles confirm the effect of wake expansion in Fig. 21 (c,d) as both profiles follow the wake's spanwise expansion. Note that the *rms* concentration profiles display the similar double-peak shape of the *rms* velocity fluctuations of Fig. 12.

The effect of shed vorticity on the scalar distribution downstream is displayed in Fig. 22. As the mid span flow region is two-dimensional, the scalar transport is mostly controlled by the production and shedding of span wise vorticity $\omega_z$. In Fig. 22 c) we observe the instantaneous vorticity and scalar concentration profiles in the vertical coordinate at two downstream locations indicated in the contour plots of Fig. 22 a). Both variables are spatially and temporally correlated as the scalar concentration maxima follow approximately the position of the maximum/minimum of $\omega_z$ vorticity. In the first position ($x/e = 20$) the scalar peak occur near the positive vorticity peak, whereas at the

second position (a half-wavelength downstream, $x/e = 30$) the scalar peak occur near the negative vorticity peak. This scalar-vorticity synchronisation relies on the ability of the wake to capture and then distribute the scalar, which makes this scalar injection mechanism particularly important. In the next case, the scalar injection was made at the span edges of the flap trying to supply a scalar flux into tip vorticity.

*4.1.3. Case 3: Tip vortex scalar injection*

In this last case the scalar injection is performed at two symmetric and slim strips (width $\Delta z = 6$ mm, or $\Delta z/e \sim 3.6$) along the two spanwise borders of the flap as indicated in Fig. 16. The objective of this configuration is to qualitatively understand the shedding of vorticity and the subsequent creation of tip vortices detaching from the flap's span edges in order to determine their capabilities to transport a given amount of scalar along the wake.

Tip vortices are normally produced at span edges in non symmetric airfoils, but in the case of a flat-plate the mechanism to produce tip vortices is by means of the accelerations of the flap, creating mainly $\omega_x$ vorticity during the upward/downward flap stroke (Bao and Tao, 2013; Jantzen et al., 2014).

We tested again the two characteristic frequencies $f_n$, $f_w$ and the first impression is that the scalar is a good tracer of the vorticity distribution. In fact, as we see in Fig. 23 the scalar is trapped by the tip vortices as long as they are rolling downstream during the forcing cycle.

The magnitude of the concentration profiles decreases downstream due to the diffusive effects. In Fig. 24 we observe how the scalar concentration decreases downstream at a given forcing frequency
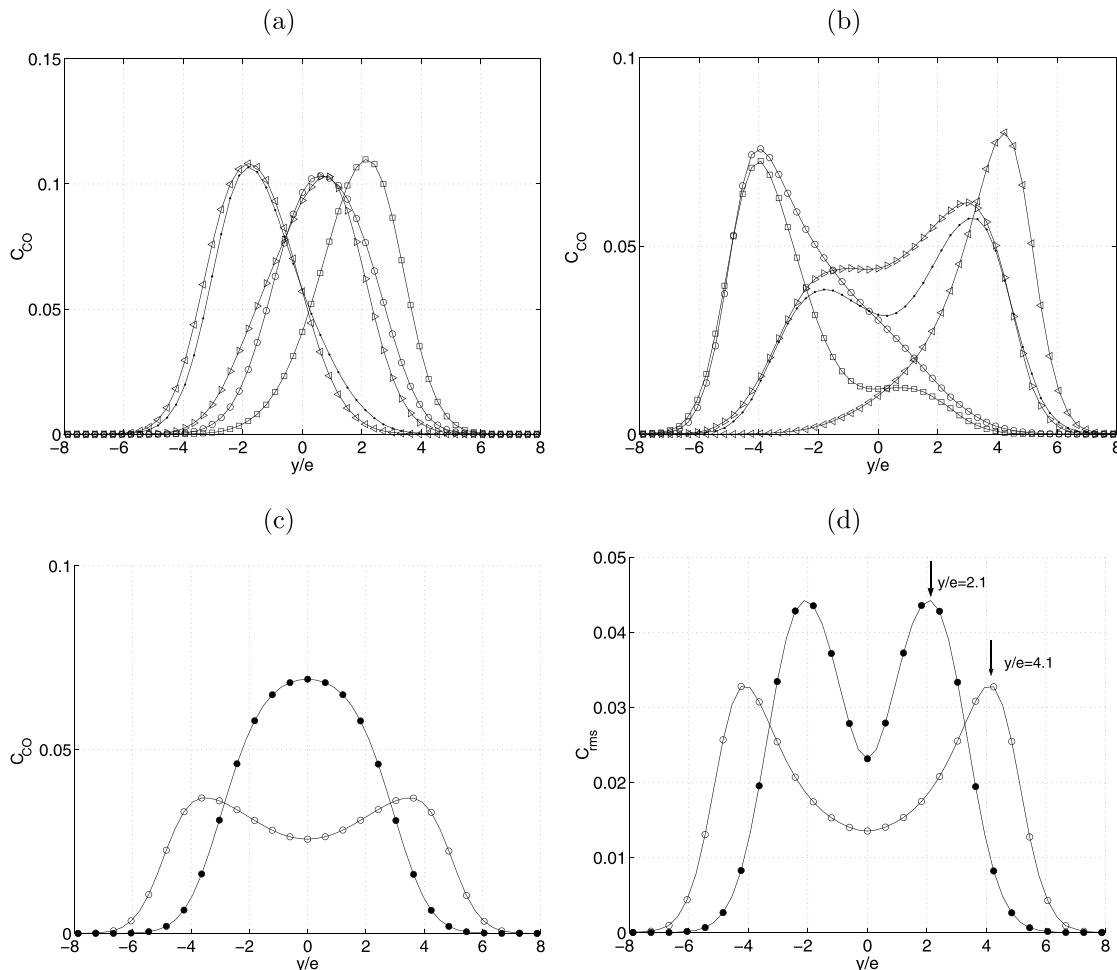


**Fig. 21.** Case 2. Scalar concentration profiles at different time instants of a single forcing cycle (• 0.2T; ∘ 0.4T; ☐ 0.6T; ▷ 0.8T; ◁ 1T) at $x/e = 30$ and $Re = 4.3 \times 10^3$. (a) $S_t = 0.4$ and (b) $S_t = 0.8$. (c) Mean and (d) *rms* concentration profiles versus $y$. (•: $S_t = 0.4$; ∘: $S_t = 0.8$).
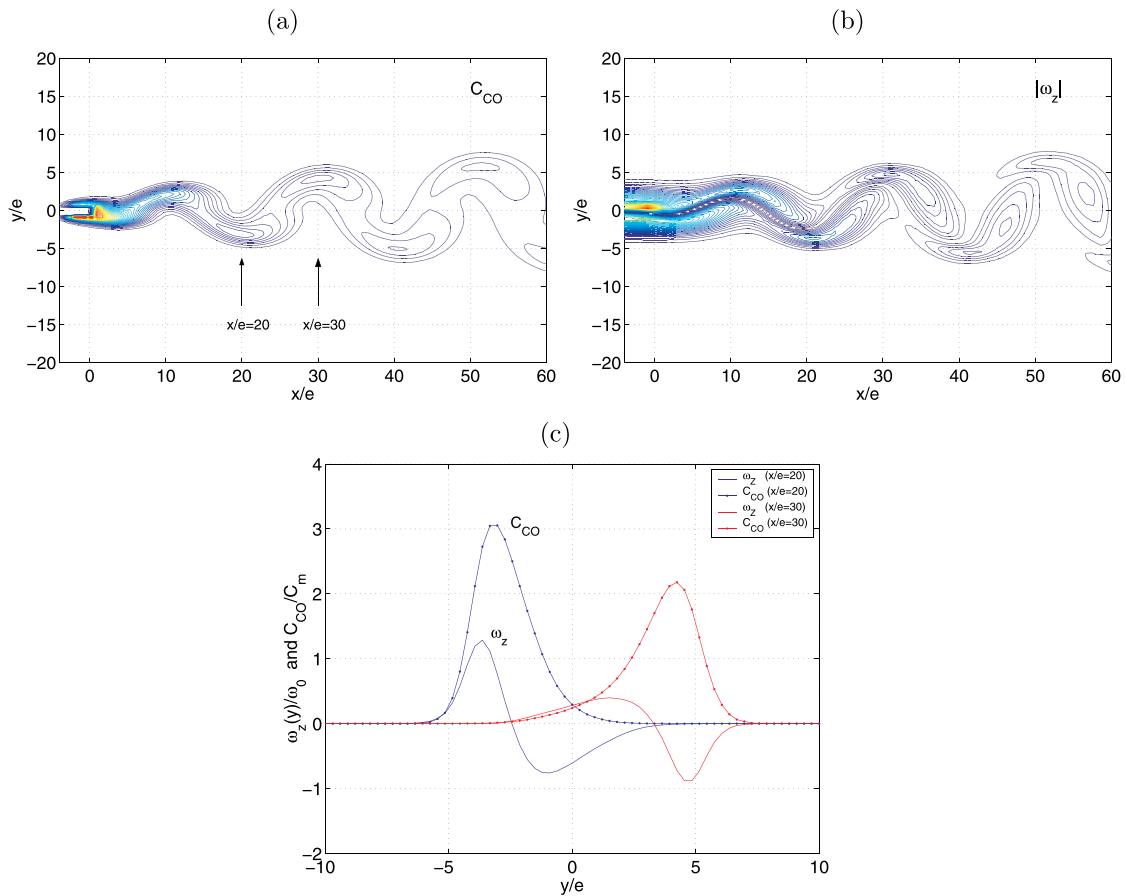
**Fig. 22.** Case 2. (a) Instantaneous scalar concentration and (b) absolute vorticity $|\omega_z|$ contours at $S_t = 0.8$ and $Re = 4.3 \times 10^3$ at mid span ($z = 0$). (c) Dimensionless vorticity and concentration profiles across the wake at two streamwise locations $x/e = 20, 30$. Here $\omega_0 \sim U_0/\delta$ and $C_m$ is the maximum value of averaged concentration profile at $S_t = 0.8$ (cf. Fig. 21 c).

($S_t = 0.8$). The characteristic thickness of the scalar profile in $z$ does not change appreciably at successive downstream locations. However, in the top view of the scalar distribution we notice a slight inwards bending towards mid span, probably due to the oscillating amplitude of tip vortices. This effect can be seen in Fig. 24 (a) where we show a top view of the scalar distribution at mid $y$ when the flap is exactly at the $y = 0$.

In both cases the scalar transport takes place localized around the borders of the flap during its downstream transport. However all the way downstream along $z$, the scalar intensity drops rapidly as shown in Fig. 24 (c,d). Wake $\omega_x$ vorticity contained in a ($y, z$) plane and the respective scalar concentration distribution seems to fluctuate coherently. It is clear that both variables are spatially correlated as their maxima occur on similar spatial locations, a result also observed in the previous case (4.1.2). This is associated to the onset and shedding of tip vortices during the forcing cycle which drives the scalar transport,

modulated spatially and in time by the pitching flap (cf. Fig. 23). As the tip vortex shedding is taking place from the borders of the flap, $z \pm s/2$ ($s$ is the flat-plate span) the $\omega_x$ vorticity intensity should increase as the result of the downward/upwards flap stroke near the flap ends. At the same time, during a single forcing duty cycle, peak vorticity contours of Fig. 25 change sign as the corresponding sign of the flap acceleration does (cf. Eq. 4). The numerical simulation, in contrast to the experiments, was performed without end-plates which allow to increase vorticity at the flap ends and therefore increase the tip vortex intensity when the flap moves. If the forcing frequency increases, the corresponding accelerations of the flap tip increase rapidly and tip vortex shedding can be produced downstream. In this process, we think that the flap acceleration during upwards/downward stroke could be a effective controlling parameter to influence (enhance/suppress) the scalar transport mediated by such vortex structures.
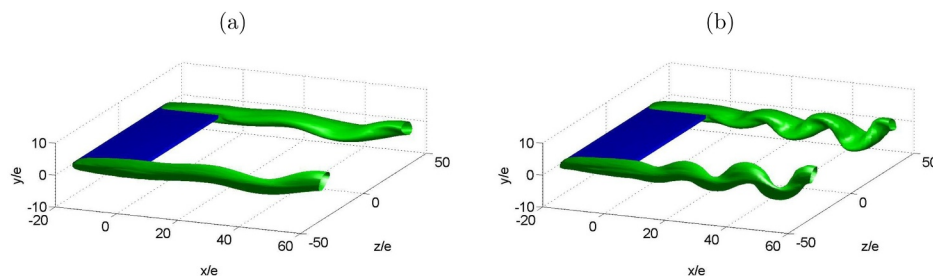


**Fig. 23.** Wake visualization in case 3 (flap in blue). Distribution of scalar $C = 0.05$ at a given duty cycle fraction $t = 0.4T$ with $T = 1/f_0$ at $Re = 4.3 \times 10^3$. (a) $S_t = 0.4$. (b) $S_t = 0.8$. (For interpretation of the references to colour in this figure legend, the reader is referred to the web version of this article.)
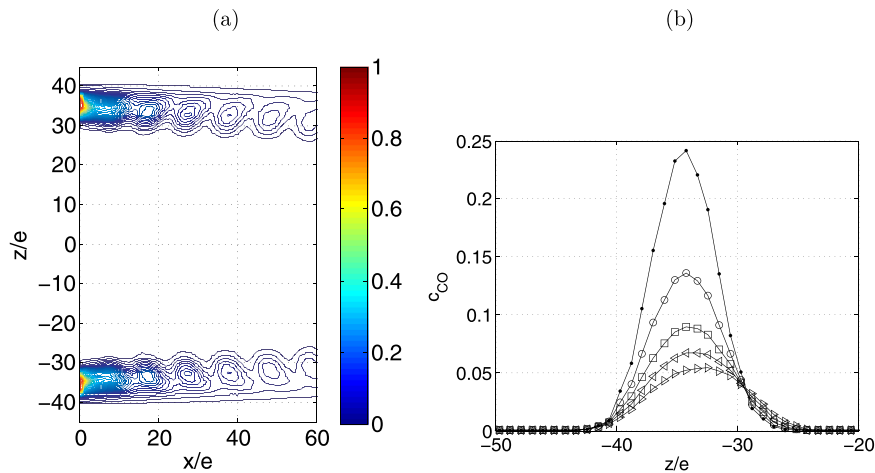
(a)                                              (b)



**Fig. 24.** Case 3. (a) Top view ($x - z$ plane at $y = 0$) of scalar concentration at $Re = 4.3 \times 10^3$. (b) Mean concentration profiles (time-averaged) at different downstream locations at $S_t = 0.8$. •: $x/e = 10$; ∘: $x/e = 20$; □: $x/e = 30$; ◁: $x/e = 40$; ▷: $x/e = 50$.

## 5. Conclusions

We performed experiments and numerical simulations in order to study the effect of a pitching flap on the wake flow dynamics of a flat-plate and its effect on scalar transport. The pitching motion of the flap introduced velocity disturbances into a initially steady wake flow which become convectively unstable. Continuous flap motion produced an unsteady wake flow in the form of a spatio-temporal oscillation at the forcing frequency imposed by the flap. Wake flow numerical simulations have been compared with our experimental results for a fixed flat-plate with a pitching flap of the same dimensions. Overall, there is a good agreement between the experiment and the numerical simulation, with a standard deviation, between wake velocity profiles, falling below 8%.

The numerical results provided a complementary view of the experimental results, allowing to identify vortex structures present and responsible of the wake dynamics, particularly useful when the flap is in motion.

In the forced flow regime, a small amplitude flap pitching triggers periodic spatio-temporal wake flow oscillations which can be predicted by a dispersion relation between forcing frequency and wake flow wavelength. We observed two particular frequencies (named $f_n$ and $f_w$), where the wake flow organises with a different topology. At $f_n < f_w$ the wake shrinks becoming very narrow and alignment of the vortex structures occurs mainly near the centerline in agreement with the literature (Hernández and Vial, 2008; Koochesfahani, 1989). Keeping the upstream velocity constant, an increase of the forcing frequency at $f_w$ make the wake to raise its centerline velocity (becomes flatter) and the spatial thickness of the velocity profile increases.

The mechanics of this particular behaviour is similar both in the experiment and the numerical simulations, but it was with the aid of the numerical results that we were able to confirm the wake response to such frequencies. We have observed an effect in the use of end-plates in the frequency response of the wake and in the values of the characteristic frequencies $f_n$, $f_w$ which may have the same origin as discussed in the work of (Williamson, 1989). The numerical simulation, in contrast to the experiments, was performed without end-plates and we think that tip vortices were shed during the forcing cycle and then modulated by the pitching flap. Tip vortex shedding was originated from the span edges of the flap where the streamwise vorticity intensity increases as the result of the flap acceleration during upwards/downward stroke at the flap ends.

At such low Reynolds numbers ($Re < 10^4$) tip vorticity has shown to have little effect on the steady state wake flow and a significant effect when the unsteady wake is responding to either of the two frequencies.

As an extension of this unsteady wake behaviour, we have solved in the numerical model the advection-diffusion equation to determine the effects of the forced wake flow on the concentration field of a given passive scalar substance like carbon monoxide, *CO*.

We studied the scalar dynamics when it is injected in particular zones of the test section. The transport and mixing dynamics of the passive scalar considered three initial scalar distributions: (i) A first case where we filled up the lower half of the control volume in the numerical simulation with *CO*, which was continuously injected at the inlet upstream. (ii) In a second case, the passive scalar substance injection occurs at the trailing edge border of the flap, and finally (iii) a third case, where the scalar was injected from two symmetric narrow strips along the two $z$ borders of the flap. The scalar concentration follows the vorticity dynamics, being both spatially and time modulated by the oscillating wake flow. The Schmidt number of the mixture was $Sc = 0.54$, i.e, which corresponds to an important diffusive effect, an unfavourable case for downstream transport.

As the numerical simulation was made to match as close as possible the experimental setup, the agreement between experiments and numerical results provided some confidence to pursuit the scalar transport study. While the experiment provided insight on the most important flow properties of the unsteady wake behaviour, the numerical runs provided a complementary picture of the flow, allowing to identify the flow structures responsible of both wake states seen at $f_n$, $f_w$ and their effect on the scalar dynamics.

The resonant behaviour of the wake manifested itself with a considerable downstream wake expansion where the scalar dynamics was deeply affected. Important effects on the transport of the scalar were observed, as the scalar injected form the flap borders is transported downstream but controlled by the action of tip vortices created during the forcing cycle.

The scalar transport across the wake flow has many similarities and share some mechanisms found on air curtains used to confine dangerous gases and temperature inside tunnel fires.

### Declaration of interests

The authors declare that they have no known competing financial interests or personal relationships that could have appeared to influence the work reported in this paper.
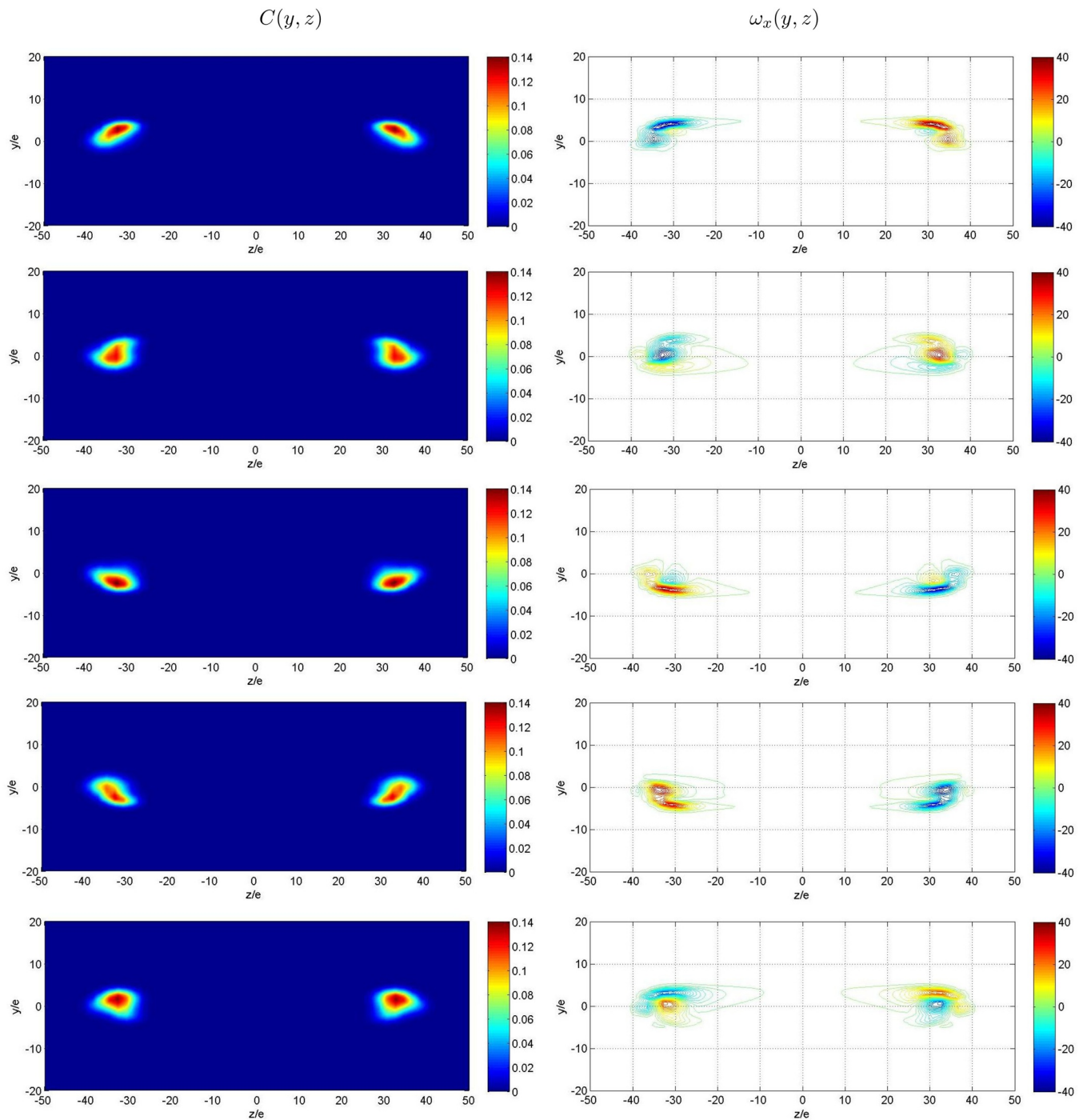
**Fig. 25.** Case 3. Cross stream views over a single forcing cycle. Scalar concentration $C(y, z, t)$ (left) and vorticity distribution $\omega_x(y, z, t)$ (right) at $x/e = 30$, $S_t = 0.8$ and $Re = 4.3 \times 10^3$. From top to bottom time instants are $t = (0, 0.2, 0.4, 0.6, 0.8) \times T$ with $T = 1/f_0$.

## CRediT authorship contribution statement

**R.H. Hernández:** Conceptualization, Formal analysis, Writing - original draft. **L. Tapia:** Conceptualization, Formal analysis, Writing - original draft.

## Acknowledgments

## Supplementary material

Supplementary material associated with this article can be found, in the online version, at 10.1016/j.ijheatfluidflow.2019.108526 .

## References

Andersen, A., Bohr, T., Schnipper, T., Walther, J.H., 2017. Wake structure and thrust generation of a flapping foil in two-dimensional flow. J. Fluid Mech. 812 (R4). https://doi.org/10.1017/jfm.2016.808.

Bao, Y., Tao, J., 2013. Active control of a cylinder wake flow by using a streamwise oscillating foil. Phys. Fluids 25 (053601). https://doi.org/10.1063/1.4802042.

Comte-Bellot, G., 1976. Hot wire anemometry. Annu. Rev. Fluid Mech. 8, 209–231.

Ehrenstein, U., 2018. Thrust and drag scaling of a rigid low-aspect pitching plate. J. Fluids Struct. 87, 39–57.

Ellington, C.P., Berg, C.V.D., Willmott, A.P., Thomas, A.L.R., 1996. Leading-edge vortices in insect flight. Nature 384, 626–630.

Fluent, 2009. ANSYS FLUENT 12 Theory Guide.

Freymouth, P., 1977. Frequency response and electronic testing for constant temperature hot-wire anemometers. J. Phys. E: Sci. Instrum. 10 (7), 705–710.

Gallegos, R.K.B., Sharma, R.N., 2017. Flags as vortex generators for heat transfer enhancement: gaps and challenges. Renew. Sustain. Energy Rev. 76, 950–962.

Gallegos, R.K.B., Sharma, R.N., 2019. Heat transfer performance of flag vortex generators in rectangular channels. Int. J. Therm. Sci. 137, 26–44.

Gharib, M., Williams-Stuber, K., 1989. Experiments on the forced wake of an airfoil. J. Fluid Mech. 208, 225–255.

Godoy-Diana, R., Aider, J.L., Wesfreid, J.E., 2008. Transitions in the wake of a flapping foil. Phys. Rev. E 77. https://doi.org/10.1103/PhysRevE.77.016308.

Hernández, R.H., Sánchez, M., 2002. Localized bénard-von kármán vortex wake packets. Europhys. Lett. 58 (2), 222–228.

Hernández, R.H., Vial, M., 2008. Frequency response of the wake of a flat plate. Europhys. Lett. 81, 64007.

Heyes, A.L., Smith, D.A.R., 2005. Modification of a wing tip vortex by vortex generators. Aerosp. Sci. Technol. 9, 469–475.

Huerre, P., Monkewitz, P.A., 1990. Local and global instabilities in spatially developing flows. Ann. Rev. Fluid Mech 22, 473–537.

Jang, D.S., Jetli, R., Acharya, S., 1986. Comparison of the PISO, SIMPLER, and SIMPLEC algorithms for the treatment of the pressure-velocity coupling in steady flow problems. Numer. Heat Transf. 10, 209–228.

Jantzen, R.T., Taira, K., Granlund, K.O., Ol, M.V., 2014. Vortex dynamics around pitching plates. Phys. Fluids 26, 53606.

Jiang, H., Cheng, L., An, H., 2018. Three-dimensional wake transition of a square cylinder. J. Fluid Mech. 842, 102–127.

Koochesfahani, M., 1989. Vortical patterns in the wake of an oscillating airfoil. AIAA J. 27 (9), 1200–1205.

Lecaros, M., Elicer-Cortés, J.C., Fuentes, A., Felis, F., 2010. On the ability of twin jets air curtains to confine heat and mass inside tunnels. Int. Commun. Heat Mass Transf. 37 (8), 970–977.

Middelberg, J.M., Barber, T.J., Leong, S.S., Byrne, K.P., Leonardi, E., 2004. Computational fluid dynamics analysis of the acoustic performance of various simple expansion chamber mufflers. Annual Conference of the Australian Acoustical Society. Australian Acoustical Society, pp. 123–128.

Negi, P.S., Vinuesa, R., Hanifi, A., Schlatter, P., Henningson, D.S., 2018. Unsteady aerodynamic effects in small-amplitude pitch oscillations of an airfoil. Int. J. Heat Fluid Flow 71, 378–391.

Patankar, S.V., 1980. Numerical Heat Transfer and Fluid Flow. Hemisphere Publishing Corporation, Washington D.C.

Polifke, W., Gentemann, A., 2004. Order and realizability of impulse response filters for accurate identification of acoustic multi-ports from transient cfd. Int. J. Acoust. Vibrations. https://doi.org/10.20855/ijav.2004.9.3163.

Press, W.H., Teukolsky, S.A., Vetterling, W.T., Flannery, B.P., 2007. Numerical Recipes, third ed. Cambridge University Press.

Ringuette, M.J., Milano, M., Gharib, M., 2007. Role of the tip vortex in the force generation of low-aspect-ratio normal flat plates. J. Fluid Mech. 581, 453–468.

Schlichting, H., 1968. Boundary Layer Theory. McGraw Hill.

Shyy, W., Trizila, P., Kang, C., Aono, H., 2009. Can tip vortices enhance lift of a flapping wing? AIAA J. 47 (2), 289–293.

Vial, M., Bellon, L., Hernández, R.H., 2004. Mechanical forcing of the wake of a flat plate. Exp. Fluids 37 (2), 168–176.

Widmann, A., Tropea, C., 2017. Reynolds number influence on the formation of vortical structures on a pitching flat plate. Interface Focus 7, 20160079.

Williamson, C.H.K., 1989. Oblique and parallel modes of vortex shedding in the wake of a circular cylinder at low Reynolds numbers. J. Fluid Mech. 206, 579–627.

Williamson, C.H.K., Govardhan, R., 2004. Vortex induced vibrations. Annu. Rev. Fluid Mech. 36, 413–455.

Wu, J., Shu, C., 2011. Numerical study of flow characteristics behind a stationary circular cylinder with a flapping plate. Phys. Fluids 23, 73601.

Xia, X., Mohseni, K., 2013. Lift evaluation of a two-dimensional pitching flat plate. Phys. Fluids 25, 91901.